JM PAPERS

Linking emitted drops to collective bursting bubbles across a wide range of bubble size distributions

Megan Mazzatenta[1] ⓘ **, Martin A. Erinin**[1] ⓘ **, Baptiste Néel**[1] ⓘ **and Luc Deike**[1,2] ⓘ

[1]Department of Mechanical and Aerospace Engineering, Princeton University, Princeton, NJ 08544, USA
[2]High Meadows Environmental Institute, Princeton University, Princeton, NJ 08544, USA
Corresponding author: Luc Deike, ldeike@princeton.edu

Bubbles entrained by breaking waves rise to the ocean surface, where they cluster before bursting and release droplets into the atmosphere. The ejected drops and dry aerosol particles, left behind after the liquid drop evaporates, affect the radiative balance of the atmosphere and can act as cloud condensation nuclei. The remaining uncertainties surrounding the sea spray emissions function motivate controlled laboratory experiments that directly measure and link collective bursting bubbles and the associated drops and sea salt aerosols. We perform experiments in artificial seawater for a wide range of bubble size distributions, measuring both bulk and surface bubble distributions (measured radii from $30\,\mu\mathrm{m}$ to 5 mm), together with the associated drop size distribution (salt aerosols and drops of measured radii from 50 nm to $500\,\mu\mathrm{m}$) to quantify the link between emitted drops and bursting surface bubbles. We evaluate how well the individual bubble bursting scaling laws describe our data across all scales and demonstrate that the measured drop production by collective bubble bursting can be represented by a single framework integrating individual bursting scaling laws over the various bubble sizes present in our experiments. We show that film drop production by bubbles between $100\,\mu\mathrm{m}$ and 1 mm describes the submicron drop production, while jet drop production by bubbles from $30\,\mu\mathrm{m}$ to 2 mm describes the production of drops larger than $1\,\mu\mathrm{m}$. Our work confirms that sea spray emission functions based on individual bursting processes are reasonably accurate as long as the surface bursting bubble size distribution is known.

Key words: air/sea interactions, aerosols/atomisation

M. Mazzatenta, M.A. Erinin, B. Néel and L. Deike

1. Introduction

When a wave breaks at sea, it entrains air bubbles below the ocean surface. Those bubbles rise back to the surface and reside for some time before bursting and ejecting drops into the atmosphere. The ejected drops can then evaporate, leaving behind ocean spray aerosol particles composed of salts, biological material and other chemicals found in the ocean. In the atmosphere, these emitted drops and corresponding dry particles affect the radiative balance and can serve as cloud condensation nuclei (Lewis & Schwartz 2004; de Leeuw *et al.* 2011; Veron 2015; Cochran *et al.* 2017).

One main difficulty of studying spray generation by bubble bursting is the range of scales involved in the related processes, from the single breaking wave of $O(1-10\,\text{m})$ to entrained bubbles of sizes $O(0.01-10\,\text{mm})$ and emitted drops of sizes $O(0.01-100\,\upmu\text{m})$. To predict ocean spray generation from knowledge of the bubble size distribution, we must understand the physical link between underwater bubbles that rise to the ocean surface, surface bubbles that cluster and burst, and the resulting drops they eject (depicted in figure 1 of Deike 2022).

Parameterisations of the sea spray generation function used in large-scale models (as reviewed by Lewis & Schwartz 2004, de Leeuw *et al.* 2011, Veron 2015), display large uncertainties of at least an order of magnitude across the full range of emitted drop sizes. These uncertainties come from the difficulty of characterising the drop formation across many processes and scales, as well as from the various empirical ways the parameterisations are developed from interpretation of field measurements or upscaling of laboratory data. In practice, the uncertainties lead to a very different sensitivity to physical parameters such as temperature (Forestieri *et al.* 2018) and directly impact the modelled radiative balance and climate sensitivity in climate models (Paulot *et al.* 2020).

Individual bubble bursting has been extensively studied to characterise the production mechanism, size and number of drops produced by the bursting of a single bubble. Previous laboratory experiments have focused either on film drops (Blanchard & Syzdek 1988; Resch & Afeti 1991, 1992; Spiel 1997*a*, 1998; Lhuissier & Villermaux 2012; Jiang *et al.* 2022) or jet drops (Spiel 1997*a*, 1998; Ghabache *et al.* 2014; Walls, Henaux & Bird 2015; Ghabache & Séon 2016; Walls, Henaux & Bird 2015; Brasz *et al.* 2018), and numerical simulations have studied jet drop production (Brasz *et al.* 2018; Deike *et al.* 2018; Berny *et al.* 2020, 2021). From those studies, scaling laws have been developed that relate the bursting bubble size to the number and size of drops emitted through jet drop production (Gañán-Calvo 2017, 2023; Blanco–Rodríguez & Gordillo 2020), film drop production through a centrifuge mechanism (Lhuissier & Villermaux 2012), and film drop production through a proposed flapping mechanism (Jiang *et al.* 2022, 2024). However, the extent to which these scaling laws, developed for idealised individual bubble bursting, apply to more realistic configurations like clusters of bubbles within ocean whitecaps, remains to be experimentally demonstrated. Combining the above-mentioned individual bubble bursting scaling laws for the various mechanisms with the bubble size distribution under a breaking wave and the statistics of air entrainment at large scale, Deike, Reichl & Paulot (2022) developed a mechanistic sea spray emissions function and demonstrated the remarkable coherence with empirically-derived emission functions. To obtain the ocean spray emission function, Deike *et al.* (2022) integrate over a given bubble size distribution (constrained by the laboratory and numerical studies of Deane & Stokes 2002; Deike, Melville & Popinet 2016; Gao, Deane & Shen 2021; Mostert, Popinet & Deike 2022), assuming individual bubble bursting scaling laws for the size, number and distribution of emitted drops for each production mechanism. The method uses the integration introduced for film drop production by Lhuissier & Villermaux (2012) and extended to jet drop

production in Berny *et al.* (2021), and air entrainment volume by breaking waves statistics in the ocean (Deike *et al.* 2016, 2017).

The approach from Deike *et al.* (2022), as well as past approaches (see the overview in Lewis & Schwartz 2004), assumes that the bubble size distribution under a breaking wave is always of the same shape and does not consider collective bubble bursting or surfactant effects. Physico-chemical properties of the ocean water – such as salinity, temperature, surfactant concentration, and biological composition – bring another layer of complexity to sea spray generation by potentially modulating the bubble processes (i.e. lifetime, coalescence, bursting). Modelling of sea spray organic aerosol emissions in Burrows *et al.* (2014) highlights the numerous chemical and biological factors that are thought to influence spray generation, showing that – despite extensive past experimental efforts – there is still a need for controlled, well-constrained experiments to improve our knowledge of how these realistic factors control the bursting processes while limiting experimental uncertainties.

To investigate the collective bursting relevant to the open ocean context, previous experiments have measured drop production by collections of bubbles generated through different methods in a variety of complex solutions, focusing especially on the measurement of submicron drops/aerosols. The experiments include bursting bubbles generated by both a plunging sheet and nucleation bubbler in natural and artificial seawater (Wang *et al.* 2017), bursting bubble rafts produced in sampled natural seawater through a forced-air venturi channel (Frossard *et al.* 2019), the investigation of the effect of phytoplankton and bacteria on aerosol production for bubbles generated by laboratory breaking waves in natural seawater (Prather *et al.* 2013), as well as several other experiments involving bursting bubble rafts or foams including those in solutions of different organic content or different salt concentration (Cipriano & Blanchard 1981; Liger-Belair & Jeandet 2003; Mårtensson *et al.* 2003; Sellegri *et al.* 2006; Tyree *et al.* 2007; Modini *et al.* 2013; Séon & Liger-Belair 2017; Zinke *et al.* 2022; Dubitsky *et al.* 2023). These studies suggest that ocean physico-chemical parameters modulate the bursting process. However, the complexity of the seawater solution and the lack of complete bulk bubble, surface bubble and drop/dry particle measurements across a wide range of scales make it difficult to compare results from separate studies and to distinguish the specific effects of individual physico-chemical variables among other differences due to varied bubble size distributions or collective bursting.

These uncertainties and their practical consequences on ocean spray emission functions motivate an intermediate-scale collective bursting laboratory experiment, measuring bubbles in the bulk and at the surface as well as the produced drops, as a way to bridge the idealised and the oceanic spray generation configurations. Using a well-characterised set-up with measurements that capture the full size range of bubbles and associated ejected drops, we can maintain precise control over the solution while observing the effect of any changes in the properties on the collective bursting. This idea was introduced through the experiments of Néel & Deike (2021); Néel *et al.* (2022), where systematic measurements of millimetric bubbles and supermicron drops were made for solutions of different surfactant concentrations.

In this paper, we perform experiments with measurements of all relevant scales of bulk and surface bubbles (radii $30\,\mu m$ to $5\,mm$), liquid drops (radii $10\,\mu m$ to $500\,\mu m$) and salt aerosols (equivalent drop radii $50\,nm$ to $10\,\mu m$) for various clustered bubble configurations, allowing us to directly characterise the link between the drop size distribution and the surface bursting bubble distribution. We have designed a bubbling tank experiment (building off the work of Néel & Deike 2021) where bubbles are generated at the bottom of the tank, and statistical measurements are made in the bulk and at

(*a*)
Narrow-2 mm

(*b*)
Narrow-3 mm

(*c*)
Narrow-250 µm

(*d*)
Broad-2 mm
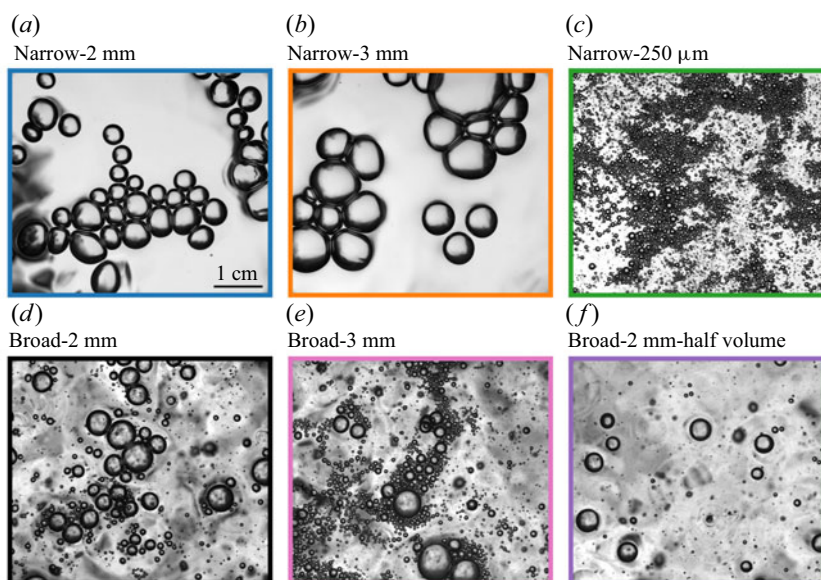
(*e*)
Broad-3 mm

(*f*)
Broad-2 mm-half volume

Figure 1. Characteristic images of bubbles on the water surface for six conditions presented in this paper. The top row shows narrower size distributions of clustered bubbles for injection sizes (*a*) 2 mm, (*b*) 3 mm and (*c*) 250 µm. The bottom row shows broad-banded distributions initially injected as (*d*, *f*) 2 mm and (*e*) 3 mm bubbles before underwater turbulence caused the breakup of these injected bubbles into those spanning a wide range of scales. In (*f*), half the volume of 2 mm bubbles were injected compared with the other cases (using 16 instead of 32 needles), leading to bubbles that are more isolated instead of clustered at the surface. Details of how bubbles were generated for each case are found in table 1.

the surface. Three measurement techniques are combined to measure drop sizes spanning four orders of magnitude: optical digital inline holography allows the measurement of drops ejected in the air with radii from 10 µm to 500 µm, while smaller droplets (not accessible with direct imaging techniques) are inferred by drying and measuring the size of the resulting salt crystals, spanning equivalent drop radii of 50 nm to 10 µm. We characterise the spray generation by clusters of bubbles in a precisely controlled solution of artificial seawater, and we vary the bulk bubble size distribution across cases. The bulk bubble size distributions tested include quasi-monodisperse plumes of rising bubbles centered around 3 mm, 2 mm and 250 µm, as well as broad-banded distributions where bubbles range from 30 µm to 3 mm. The broad-banded size distributions mimic the bubble size distribution entrained by breaking waves. As illustrated in figure 1, these bubble size distributions exhibit very different characteristics at the surface, which will control the resulting drop size distribution. We then explore whether we can describe the associated spray generation by these various bubble distributions within a single physical framework.

The paper is organised as follows. We detail the set-up, experimental methods, and resulting size distribution data in § 2. In § 3, we discuss linking the bulk bubble and surface bubble measurements, followed by the § 4 analysis linking the surface bubble and drop measurements. Section 5 presents the conclusions.

2. Measuring bubbles, drops and dry particles in a bubbling tank

We present the experimental methods, including a description of the bubbling tank, preparation of the artificial seawater solution, measurements of bulk bubbles,

surface bubbles and finally drops/dry particles. Sample size distributions from these measurements are then shown and discussed.

2.1. *Experimental set-up and conditions*

The experimental set-up, shown in figure 2, consists of a polycarbonate tank with inner dimensions $47 \times 47 \times 61 \text{ cm}^3$, similar to the one used by Néel & Deike (2021), which is filled to a height of 35 cm with a solution of artificial seawater (made of deionised (DI) water and artificial sea salt, ASTM D1141-98, Lake Products Company LLC). The water height is chosen so that the waves/fluctuations on the water surface remain small and the surface bubbles can be clearly imaged. Bubbles are continuously generated as compressed air flows through the needles positioned at the bottom of the tank, arranged in a square with eight needles extending horizontally from each side. The air flow rate through the needles is controlled at $100 \text{ cm}^3 \text{ min}^{-1}$ per needle, so that the resulting plume of rising bubbles is fairly monodisperse.

The artificial seawater solution is prepared by mixing DI water with ASTM D1141-98 artificial sea salt, which contains the same proportions of elements found in natural seawater in amounts greater than 0.0004 % by weight (Lake Products Company LLC). Solutions discussed in this paper were prepared with a salinity of 36 g L^{-1} (35 g kg^{-1}) to mimic the composition of ocean water. The solution has liquid viscosity $\mu = 1.001 \text{ mPa s}$, liquid density $\rho = 1025 \text{ kg m}^{-3}$ and static surface tension $\gamma = 52 \text{ mN m}^{-1}$. The low static surface tension indicates that the salt mixture likely includes some surfactant. At the beginning and end of each day of experiments, the solution was characterised by measuring the surface tension isotherm with a Langmuir trough (KSV NIMA, model KN 1003). This measurement was used to confirm that the surface properties of the solution remained consistent over multiple days of experiments.

Two pumps (Rule 20 DA 800 GPH Bilge Pump) are mounted 6 cm above the needle tips, pointed towards each other from opposite corners. When the pumps are turned on, they produce water jets that meet in the center of the tank, creating a region of turbulent flow that causes the rising bubbles to fragment into many smaller bubbles, with turbulence similar to the set-up described in Ruth *et al.* (2022). Experiments can be performed with or without forced turbulence, where the turbulence has two effects: agitate the flow and break the bubbles, leading to a broad-banded size distribution. Note that bubble imaging occurs above the region of active breakup.

Three experimental parameters were varied to create different initial bubble size distributions for the different cases run in this experiment: turning the underwater pumps off or on to create either a narrow- or broad-banded bulk bubble distribution, changing the needle size/bubble production method, and reducing the number of needles (which effectively reduces the injected air volume per unit time because the flow rate per needle is kept constant). An aquarium bubbler is also used to generate a plume of submillimetric bubbles centered around 250 μm.

Figure 1 illustrates the wide range of surface bubble populations explored in this paper, showing representative images of the various conditions detailed in table 1. The surface bubble distributions display marked differences in terms of both sizes and clustering, which will control the emitted drop size distribution. There are also significant differences in the number of bubbles present at the surface in each condition, which are associated with very different numbers of produced drops (see Appendix A for the total number of drops compared with the number of bubbles for each case). Because of the variety in size, number, and clustering of surface bubbles for various conditions, it is necessary to
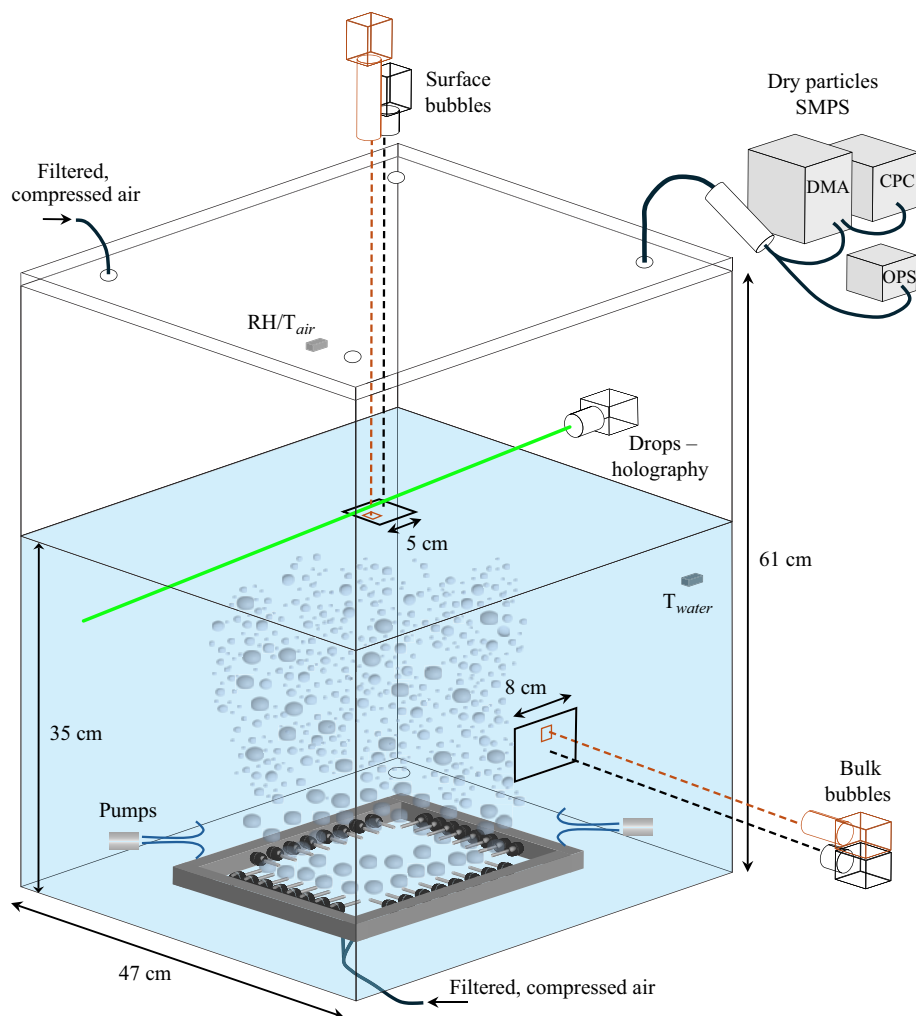
Figure 2. Sketch of the experimental set-up, with measurements of bubbles, drops and dry aerosol particles. Bubbles of nearly identical sizes are generated by compressed air flowing through needles at the bottom of the tank. When two underwater pumps are turned on (as illustrated in the sketch), the injected bubbles are broken up into many smaller bubbles as they rise into the region of turbulence generated by the water jets from the pumps (bubbles not drawn to scale). The bubbles are imaged from the side view to measure the rising bulk bubbles and from the top view to capture the bubbles at the surface. Large fields of view (black) and small fields of view (orange) are drawn approximately to scale and permit the measurement of bubble radii from 30 μm to 5 mm. Liquid drops ejected into the air by bursting bubbles are measured through an inline holographic set-up (measuring liquid drop radii from 10 μm to 500 μm), while dry aerosol particles are measured by extracting and drying the liquid drops and analysing them using an optical particle sizer (OPS) and scanning mobility particle sizer (SMPS, composed of a differential mobility analyzer (DMA) and a condensation particle counter (CPC)) (for dry particle radii from 20 nm to 5 μm). A line of filtered, compressed air is connected to the lid to flush the air above the water surface before the start of each run. Relative humidity and both air and water temperature are monitored throughout the experiments.

characterise the surface properly through many measurements, across all scales, before attempting to link the bursting surface bubbles to the drops they produce.

In order to capture the large range of length scales present in the system – spanning bubble radii of 30–5000 μm and drop sizes of 0.05–500 μm – we make multiple

Case description	Bubble Production Method	Total air Flow rate (cm^3 min^{-1})	Needle ID (μm)	Pumps	No. Needles	$R_{b,inj}$ (mm)	$n_{R_b < 2\,\text{mm}}$ (cm^{-3})
Narrow-2 mm	Needles	3200	432	Off	32	2	0.40
Broad-2 mm	Needles	3200	432	On	32	2	45
Broad-2 mm-half volume	Needles	1600	432	On	16	2	25
Narrow-3 mm	Needles	3200	965	Off	16	3	0.13
Broad-3 mm	Needles	3200	965	On	32	3	43
Narrow-250 μm	Porous media (Bubbler)	800		Off		0.25	57

Table 1. Experimental parameters. The bulk bubble size distribution across cases was varied by changing between quiescent and turbulent flow underwater (by turning the underwater pumps off or on, causing the bubbles to break up in the turbulent case), by changing the injection bubble size (using two different needle sizes or an aquarium bubbler) and by halving the volume (using 16 instead of 32 needles with the same air flow rate per needle). Case names describe the range of radii over which a significant number of bubbles are concentrated (narrow, broad) and the initial injection bubble size before any breakup in turbulence (2 mm, 3 mm, 250 μm). The broad-2 mm-half volume case is characterised by bubbles arriving at the surface isolated from each other, bursting individually instead of clustered as the smaller number of needles leads to both a reduced volume and increased needle spacing. Here $R_{b,inj}$ represents the typical injection bubble size by the needles or bubbler; $n_{R_b < 2\,\text{mm}}$ shows the number of bubbles (per unit volume) smaller than radius 2 mm, which reinforces the designation of certain cases as narrow- or broad-banded. We provide the total air flow rate through the needles for each case, but we caution that this flow rate value should not be used to approximate the bubble population in our configuration, as it is primarily related to the volume contained in the largest bubbles and does not capture the variations in the bubble size distributions (broad and narrow configurations) necessary when linking bursting bubbles to emitted drops. Bubble size distributions for each case are shown throughout §§ 2.2.4, 4.1 and 4.2. Representative surface bubble images for each case are shown in figure 1.

measurements of bulk bubbles, surface bubbles, drops and dry particles. Bulk bubbles are imaged in both a large and small field of view by cameras positioned above the region of active breakup. Surface bubbles are also captured in two fields of view by cameras positioned perpendicular to the water surface, where the bubbles cluster near the center of the tank before bursting and ejecting drops into the air above the water surface, which is enclosed in the tank with an acrylic lid.

Drops are sized using a combination of an inline holographic system positioned just above the water surface (Erinin *et al.* 2019, 2023), an optical particle sizer (OPS from TSI, Inc., OPS 3330), and a scanning mobility particle sizer (SMPS from TSI, Inc., which consists of an advanced aerosol neutralizer, model 3088; an electrostatic classifier, model 3082; a differential mobility analyzer, model 3081; and a condensation particle counter (CPC), model 3752). The SMPS operates with an aerosol flow rate of 0.3 L min^{-1} and sheath flow rate of 2.4 L min^{-1}. The OPS and SMPS are connected through the lid and pull air with suspended drops out of the tank, where they are dried (TSI diffusion dryer, model 3062) and then measured. Relative humidity and air temperature are monitored 25 cm above the calm water surface throughout all experimental runs, along with the temperature of the solution.

2.2. *Experimental protocol and statistically steady-state measurements of bubbles, drops and particles*

We present the systematic experimental protocol used to characterize drop production by bubble bursting in the statistically steady-state bubbling tank. Figure 3 illustrates the time series of the various measurements for a typical case (broad-2 mm: broad-banded
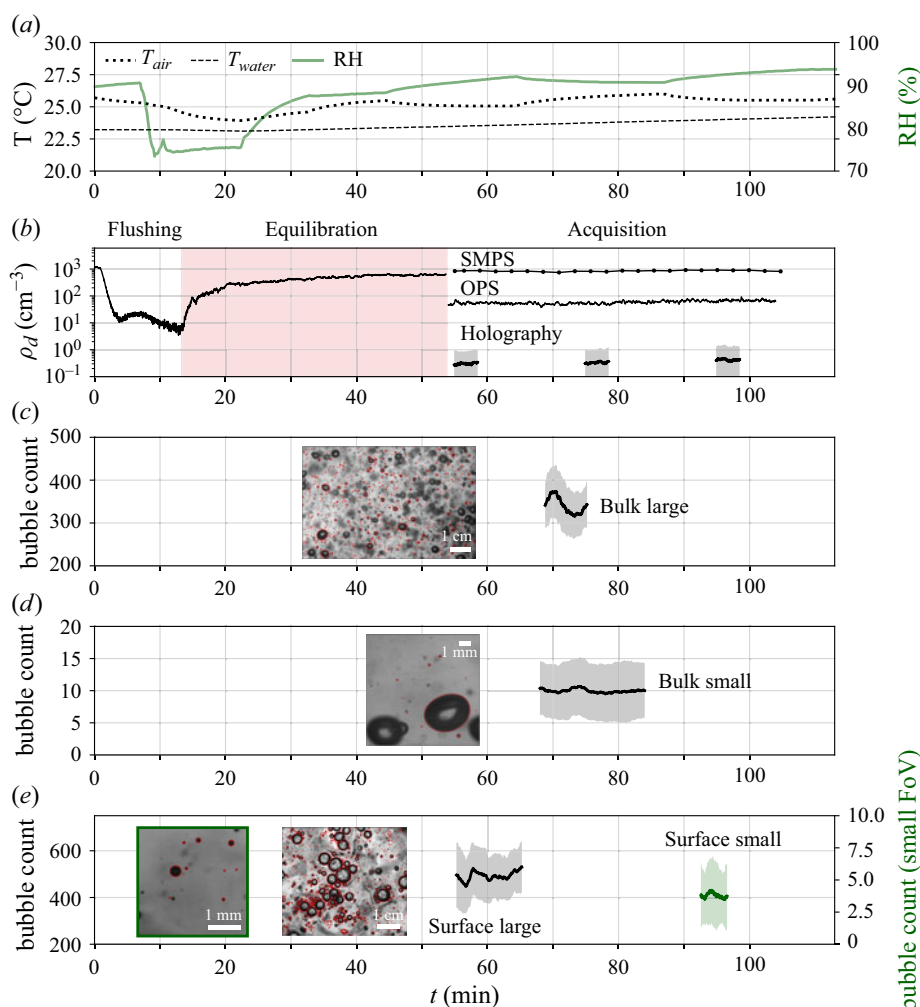
Figure 3. Experimental protocol for data acquisition illustrated by typical time series of temperature, relative humidity, bubbles, drops and dry particles through a single run on a representative case (broad-2 mm in table 1). Sample images are shown with bubble detection overlaid in red (*c–e*). Scale bars (shown as white lines on images) represent 1 cm for the bulk and surface large fields of view (*c*, right image in *e*) and 1 mm for the small fields of view (*d*, left image in e). Panel (*a*) illustrates the steps in the experimental protocol, showing first flushing to obtain clean air, followed by equilibration during which the relative humidity reaches a value of about 90 %, followed by a steady state. Air and water temperature are also shown in (*a*). The dry aerosol particle counts are shown in (*b*), with the SMPS particle count close to 0 (less than 10 particles per cm^3) at the end of the flushing stage, and reaching a steady state during the acquisition stage. Drop measurements from the holography are shown in (*b*) by a concentration ρ_d (number per measurement volume), with the rolling mean and standard deviation plotted for each holographic measurement. For the bubble measurements in panels (*c–e*), the lines represent the rolling mean of the count of bubbles detected in each frame, with shading for the rolling standard deviation. All rolling quantities were computed using a window size equal to 20 % of the total number of frames in each dataset. Each measurement shows some fluctuations around a rolling mean that remains relatively steady throughout the measurement period.

Measurement	Pixel size (µm)	Field of view (mm²)	Depth of field (mm)	Recording frame rate (Hz)
Bulk	42	80.6 × 50.4	14–26	1
Bulk small	5.3	10.6 × 10.6	2	2
Surface	10	53.3 × 46.1		2
Surface small	1.6	3.28 × 3.28		3
Drops – holography	0.98	3.89 × 2.19	360	20
Drops – shadow	29	59.4 × 59.4	120	5

Table 2. Measurement details for imaging of bulk bubbles, surface bubbles, and drops (holography and shadow) in the present experiment. The shadow imaging drop measurement was performed for certain cases (narrow-2 mm, narrow-3 mm, narrow-250 µm and broad-2 mm) to allow for the measurement of drops very close to the surface. A range is specified for the depth of field of the bulk measurement resulting from the size-dependent depth-of-field correction, and this range corresponds to the depth of field of bubble radii in the range $R_b = [150, 3000]$ µm (see details in § 2.2.3 and figure 6 of Erinin *et al.* (2023)).

distribution of bubbles created by underwater turbulence that breaks the bubbles into many smaller sizes).

Once the artificial seawater solution is in the tank, a lid is placed on top to seal the system. A constant stream of filtered, compressed air is then flowed through the air above the water surface to flush aerosols from the system. The background aerosols escape through a single port in the lid, which is left open throughout the run to maintain equilibrium within the system. The flushing continues until the CPC component of the SMPS measures a particle count below 10 particles cm^{-3}, as shown in figure 3(*b*), which can be compared with an ambient particle count of approximately 1000 particles cm^{-3}. This ensures that the sea salt aerosols we sample in the air are nearly all emitted by bubble bursting. The air through the top of the tank is then turned off, and the system is left to equilibrate for 40 mins. The CPC particle counts from the pre-run period are shown in figure 3(*b*). We confirm that the particle count and relative humidity level (figure 3*a*) have reached a steady state before proceeding with the run. Relative humidity, air temperature and water temperature are tracked throughout the run using a Thorlabs sensor (TSP01, TSP-TH) mounted to the tank lid. Values are comparable to realistic ocean conditions and remain steady throughout the run (temperatures vary by approximately 1 °C throughout the measurement period).

After the system reaches a steady state of particle counts, the SMPS, OPS, and holographic measurements begin simultaneously (shown in terms of the drop concentration in figure 3*b*). The SMPS and OPS sample continuously throughout the entire 50 min run. Three independent holographic movies are recorded during the run, with approximately 15 mins of saving time required between each measurement. For the bubbles (figure 3*c,d,e*), the large field-of-view surface measurement is made at the start of the run, followed by simultaneous measurements of bulk bubbles for both fields of view. Surface and bulk bubbles are recorded separately so that the backlighting for each measurement does not interfere with the other. Finally, the small field-of-view surface measurement is made at the end of the run. Compared with the large surface measurement, the small surface images provide a significantly more zoomed-in view that requires more light than the large surface view, so the two measurements are made separately. Details of each measurement are given below and summarised in table 2. Representative sample images for each bubble measurement are also shown in figure 3(*c–e*) with detection overlaid. Some fluctuations are present in the number of bubbles and drops with time,

but the magnitude of the fluctuations is fairly consistent throughout the run. Therefore, we consider the system to be running in a statistically steady state.

2.2.1. *Details of bulk bubbles*

As introduced for the experimental set-up in § 2.1, two cameras measure the bulk bubbles simultaneously with two overlapping fields of view to enable measurement of bubbles with radii spanning $R_b = [30, 5000]\,\mu\text{m}$ (large field of view: Basler acA1920-40 with Zeiss Planar T50 lens; small field of view: Basler acA2040-90 with Nikon AF-Micro Nikkor 200 lens and 36 mm extension tube). The recording frame rates of 1 Hz (large) and 2 Hz (small) are chosen so that a single bubble does not appear in multiple frames. Imaging details are provided in table 2.

Bulk bubble edge detection was performed using a Canny filter algorithm, which was done in multiple stages for the large field of view to enable successful detection of many sizes of bubbles. An ellipse was fit to each detected region, and the bubble radius R_b represents the volume-equivalent size of the bulk bubble, assuming axisymmetry around the minor axis of the ellipse. The void fraction ϕ_b is typically between $0.1-0.5\,\%$ for all cases studied, indicating a dilute region of bubbly flow. Through inspection of dedicated high-speed movies, we confirm that underwater collisions and coalescence in the bulk are very rare. The presence of salt limits the coalescence efficiency so that if bubbles do contact each other, they typically bounce off and do not coalesce.

The depth of field for all cases is calibrated to account for its dependence on the size of the bubble, using the method detailed in § 2.2.3 and figure 6 of Erinin *et al.* (2023). For the narrow-2 mm and narrow-3 mm cases, the depth of field is additionally adjusted to account for the fact that the bulk bubbles are not evenly distributed throughout the depth (because they are rising from a square array of needles). This adjustment leads to a larger effective depth of field for the narrow-banded cases, which enables comparison to the broad-banded cases where the bubbles are distributed evenly throughout the volume by the underwater pumps. The average relative error on the bubble radius measurement is 6 % at the limits of the depth of field; see Erinin *et al.* (2023, § 2.2.3 and figure 7).

2.2.2. *Details of surface bubbles*

At the surface, measurements of the bubbles are again made in two overlapping fields of view for the same range of bubble radii, $R_b = [30, 5000]\,\mu\text{m}$. The camera for the large field of view (Basler a2A5328–15) captures clusters of bubbles, while the small field-of-view camera (Basler acA2040-90 with Infinity K2 DistaMax microscope lens) zooms in on the smallest bubbles that rise to the surface. The large and small surface measurements were made at 2 Hz and 3 Hz, respectively, and the frame independence of both measurements was checked by downsampling in time. Details are provided in table 2.

Surface bubbles are detected using the Hough transform with custom filtering to remove duplicates and misdetection, which enabled detection of both clustered and isolated bubbles within the same frame using a single processing algorithm. The apparent radius of the detected bubbles from the surface measurement is then converted to the volume-equivalent radius R_b by considering the static shape of the bubble at the surface, as described in Néel & Deike (2021), based on the work of Toba (1959).

2.2.3. *Details of drops and dry particles*

As the bubbles burst at the surface, they release drops into the air above the water surface. Three techniques are combined to measure ejected drops with radii spanning four orders of magnitude, in the range $r_d = [0.05, 500]\,\mu\text{m}$. The first measurement is the digital inline

holographic imaging set-up (laser: CrystalLaser Nd:YLF QL527-200-L; camera: Phantom VEO4K-990-L; lens: Infinity K2 DistaMax, fully described in Erinin *et al.* 2023). The holographic set-up is positioned 5.5 cm above the water surface and captures the large sizes of drops in the range $r_d = [10, 500]\,\mu$m. The small field of view and frame rate of 20 Hz are chosen so that each drop is counted only once, either on the upward or downward part of its trajectory.

Drops are then sucked out of the air above the tank and dried. The dry salt particles in the intermediate range of dry particle diameter, $D_p = [0.3, 10]\,\mu$m, are counted and sized by the OPS. To improve the accuracy of the particle size measurement, an index of refraction of $1.5 - 0i$ is specified for the sea salt and the 660 nm laser of the OPS (Shettle & Fenn 1979). The SMPS measures the smallest particles in the range $D_p = [0.02, 0.8]\,\mu$m. The SMPS and OPS measurements have been used for atmospheric applications where the measured particle itself was of interest (Prather *et al.* 2013; Wang *et al.* 2017), as well as in other bubble bursting experiments where the OPS and SMPS measurements of salt particles are used to access the smallest sizes of drops that we are unable to measure using traditional optical methods (Sampath *et al.* 2019; Jiang *et al.* 2022; Dubitsky *et al.* 2023). To plot all three drop/aerosol measurements together, we convert the SMPS and OPS measurements of the dry particle diameter to drop radii by assuming conservation of salt mass in the drop and solving for the drop radius: $r_d = (1/2)D_p(\rho_{dry}/\rho_s)^{1/3}$. From $\rho_s = 36\,\mathrm{g\,L^{-1}}$ and $\rho_{dry} = 2{,}056\,\mathrm{g\,L^{-1}}$, we have $r_d \approx 2D_p$, as discussed in Lewis & Schwartz (2004), which is a relation classically used to convert between the salt dry particle size and the liquid drop radius.

To quantify the background noise of aerosols remaining in the system, SMPS and OPS measurements were performed for a solution of DI water immediately before each artificial seawater case is run. The calculated background is then subtracted from the size distribution, smoothed using a Savitzky-Golay filter, and cut to the trusted measurement region. In order for all three measurements to be plotted together, the native units output by the SMPS are converted to the normalised concentration $N_d(r_d)$, such that integrating the distribution gives a number of particles per unit volume (see Erinin *et al.* (2023) for conversion details).

We note that some drops above $r_d = 200\,\mu$m may not be detected by the holographic measurement because they fall back to the surface before reaching the measurement region (Néel & Deike 2022). To confirm the presence of these large drops, the drop measurements were supplemented with a shadow imaging measurement (for drops of radii $r_d > 150\,\mu$m) for the narrow-2 mm, narrow-3 mm, narrow-250 μm and broad-2 mm cases. This measurement was added directly above the level of the water surface to quantify large drops that may not have reached the holographic measurement region (camera: Basler acA2040-90; telecentric lens: Opto-E TC4MHR096-C). Details of the shadow measurement are included in table 2, and the imaging set-up is described for drop measurements in Erinin *et al.* (2023).

2.2.4. *Typical bubble and drop size distributions*

The systematic measurements described above for a wide range of scales allow us to extract full size distributions for both drops and bubbles and probe different conditions in a systematic way (conditions summarised in table 1, with sample surface images in figure 1). We illustrate the characterisation of the size distribution for two representative cases in figure 4, the broad-2 mm and narrow-2 mm cases.

Using bubble sizes and counts extracted from the images through the methods described in the previous sections, we plot the size distributions of the detected bulk and surface
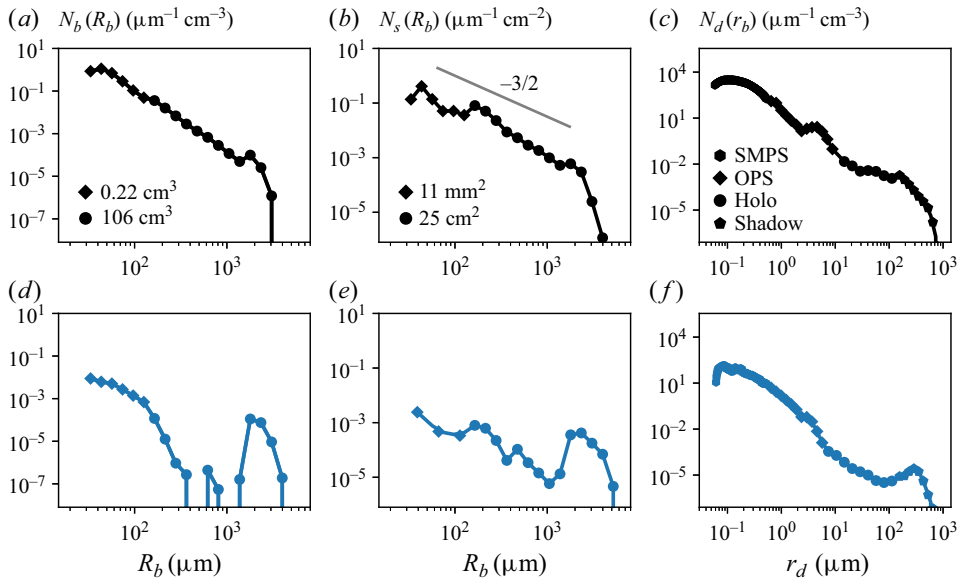
Figure 4. Size distributions of bulk bubbles, $N_b(R_b)$ (*a*,*d*), surface bubbles, $N_s(R_b)$ (*b*,*e*) and drops, $N_d(r_d)$ (*c*,*f*) for broad-banded (*a*–*c*) and narrow-banded (*d*–*f*) distributions of rising bubbles (see cases broad-2 mm and narrow-2 mm in table 1). Different symbols indicate the different fields of view (bubble measurements) or the different measurement techniques (drop/particle measurements). The drop size distribution is shown in terms of the liquid drop radius, r_d. All distributions are interpolated over the logarithmically-spaced bins, with the interpolated distribution plotted over the data points.

bubbles, $N_b(R_b)$ and $N_s(R_b)$, shown in figure 4, normalised by the bin size and by the measurement volume or area, respectively. For both bubble size distributions, data from the large and small field-of-view measurements are represented by different symbols and nicely overlap. Note that the bubble radius R_b represents the volumetric bubble radius for both the bulk and surface measurements.

For the drop size distribution, all measurements are expressed as $N_d(r_d)$, the number of drops per unit bin size and unit measurement volume. Data from the SMPS, OPS, holographic imaging, and shadow imaging overlap well, and the combined measurements result in a single distribution that characterizes drops spanning 50 nm to 500 μm. For the broad-banded case, we observe a continuum of bubble radii spanning $R_b = [30, 5000]$ μm in both the bulk and the surface (figure 4*a*,*b*). We see a corresponding continuum of drop radii spanning $r_d = [0.05, 500]$ μm (figure 4*c*). In the narrow-banded case, we see a narrow peak of bubble sizes around the injection bubble radius, $R_b = 2.3$ mm (figure 4*d*,*e*). We refer to this case as narrow-banded, or nearly monodisperse, because the majority of bubbles are found in this peak around 2 mm. Some amount of smaller bubbles are also present for this narrow-banded case (formed as bubbles pinch off from the needles), and there are also smaller drops, shown in the drop size distribution below $r_d \sim 200$ μm (figure 4*f*). The bulk and surface distributions show similar trends in both conditions, suggesting limited coalescence (which is expected for artificial seawater).

2.3. *Summary of the experimental analysis*

Having obtained the full size distributions of bubbles and drops, we now analyse the link between the different measurements to systematically quantify the attribution of drops to bursting surface bubbles. In § 3 we link the measured bulk bubble size distribution (which
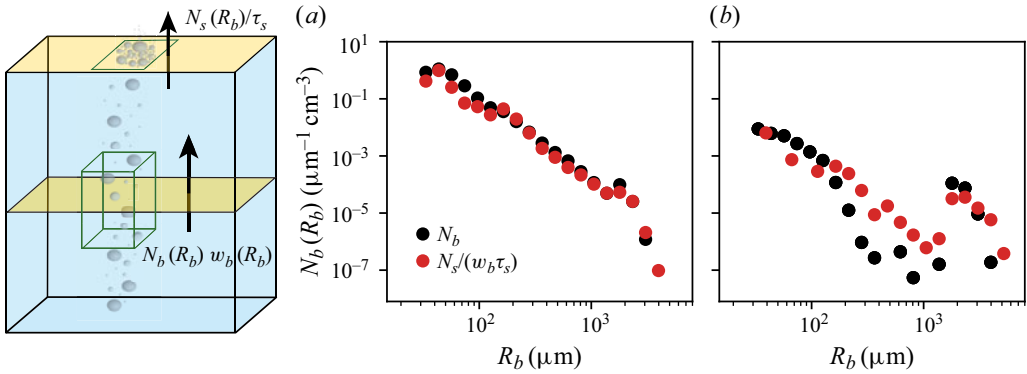
Figure 5. Comparison of the measured bulk bubble size distribution $N_b(R_b)$ to the converted surface bubble size distribution, which is represented as a quantity normalised by a measurement volume following (3.1). The comparison is shown for the medium bubble size cases of (*a*) broad-banded and (*b*) narrow-banded bulk bubble size distributions. The sketch illustrates the bulk measurement volume and surface measurement area (outlined in green, not to scale), as well as the fluxes through planes in the bulk ($N_b(R_b)w_b$) and at the surface ($N_s(R_b)/\tau_s$). Bubbles and drops not drawn to scale.

integrates to a number per unit volume) with the surface bubble size distribution (which integrates to a number per unit area) using a simple flux argument involving the bubble rise velocity and the bubble lifetime at the surface. We then analyse the link between bursting bubbles and drops in § 4. We consider a direct attribution of measured drops to measured bubbles in § 4.1, and in § 4.2 we predict a drop size distribution from the measured bubbles using existing scaling laws developed for individual bubble bursting.

3. Linking bulk and surface bubble size distributions

We now quantitatively connect the bulk bubble and surface bubble size distributions. The size distribution of bubbles bursting at the surface may evolve from the distribution seen in the bulk due to factors like coalescence, formation of child bubbles after bursting, and size-dependent time scales associated with the rising and bursting of the bubbles. For the artificial seawater solution used in this experiment, we demonstrate that the surface and bulk distributions can be related through simple assumptions used to equate a flux of bubbles through a plane in the bulk to a flux of bubbles at the surface, as illustrated by the sketch in figure 5.

The surface bubbles are measured over an area, so that $N_s(R_b)$ is a number per unit bin size per unit area, while the bulk bubbles are measured in a volume underwater, so that $N_b(R_b)$ is a number per unit bin size per unit volume. To link the two, we equate the flux of bubbles that rise through a plane underwater, $N_b(R_b)w_b(R_b)$, to a flux of bubbles arriving and bursting at the surface, $N_s(R_b)/\tau_s$, where $w_b(R_b)$ is the bubble rise velocity and τ_s the bubble lifetime at the surface. The link between the two distributions reads

$$N_b(R_b) = \frac{N_s(R_b)}{\tau_s \, w_b(R_b)}. \tag{3.1}$$

The bubble rise velocity $w_b(R_b)$ is a function of the bubble size, and we use the semi-empirical rise velocity parameterisation for contaminated water presented in Clift, Grace & Weber (1978, p. 172). The time scale required for the flux of surface bubbles is the bubble lifetime τ_s. Significant uncertainty remains surrounding the dependence of bubble lifetime on the bubble size and properties of the solution (see table 1 in Poulain,

Villermaux & Bourouiba 2018), so for simplicity, we consider a reasonable estimate of a constant bubble lifetime of $O(1)$ second (we assume that $\tau_s = 0.6$ s). Equation (3.1) effectively neglects the effect of coalescence at the surface, which is generally an appropriate simplification given the seawater salinity of the solution (effect of salts on bubble coalescence reviewed in Firouzi, Howes & Nguyen 2015).

The comparison between the bulk size distribution and converted surface distribution (calculated using (3.1)) are shown in figure 5 for the two typical cases presented in the previous section (figure 4 , broad-2 mm and narrow-2 mm). We see good agreement in the overall trends and magnitudes of the measured bulk distributions and the converted surface distributions for both the (*a*) broad-banded case with turbulence present and (*b*) narrow-banded distributions with no turbulent flow. This indicates that, for this configuration, (i) coalescence is not a dominant process to account for, and (ii) a constant τ_s is a reasonable approximation.

Some words of caution are required when presenting the flux-based comparison. We have chosen one particular rise velocity parameterisation and a constant bubble lifetime to evaluate the flux argument. Other relations for the rise velocity were also tested, including the parameterisation from Woolf & Thorpe (1991) that gives a similar result aside from a slightly different velocity for the smallest bubbles. We could also have considered the effect of the background turbulence on the rise velocity, which systematically slows down the rise velocity of the bubbles (Ruth *et al.* 2021; Liu *et al.* 2024) (we note that a systematically lower rise velocity could be compensated for by a slightly higher value of the bubble lifetime, within the uncertainties of experimentally measured bubble lifetime). Note that by integrating $\int_A (\int_{R_{b1}}^{R_{b2}} N_b(R_b)(4/3)\pi R_b^3 w_b(R_b) \, \mathrm{d}R_b) \, \mathrm{d}A$ over the total range of bubbles sizes $[R_{b1}, R_{b2}]$ and the area A of the plane through which the bubbles rise, we do obtain air flow rates that are consistent with the total prescribed air flow rate given in table 1 (and controlled primarily by the largest bubbles). By assuming (3.1) and a rise velocity function, we could also have extracted an effective bubble lifetime function. While uncertainty remains in both the chosen rise velocity and lifetime, we find that we can relate the bulk and surface bubble size distributions well for all the cases presented in the paper, so that we can use the bulk and surface measurements interchangeably by applying (3.1).

In the following analysis, we use an effective size distribution for bursting bubbles (using both surface and bulk data) to practically relate the bubbles to the drop size distribution, which is measured per unit volume. A direct link between bursting bubbles and emitted drops in terms of fluxes would require measurements of the drop velocity (not available here). To come up with this effective bubble size distribution, the surface bubble distribution is first converted to a quantity of bursting bubbles normalised by a volume, following (3.1). For bubbles below $R_b = 150 \, \mu$m, we use data from the bulk small field-of-view measurement to construct a complete size distribution of bubbles spanning $R_b = [30, 5000] \, \mu$m. Throughout the rest of the paper, the term $N_b(R_b)$ is used to represent this size distribution of bursting bubbles from the combined measurements, with the exception of the narrow-250 μm case, which uses only the converted surface data due to imaging/detection difficulties for bubbles in the denser bulk plume.

4. Linking drops and bursting bubbles

We can now analyse the link between the surface bubbles and ejected drops in the collective bursting configuration by examining how the drop size distribution changes as the bubble size distribution is intentionally varied through the different cases.
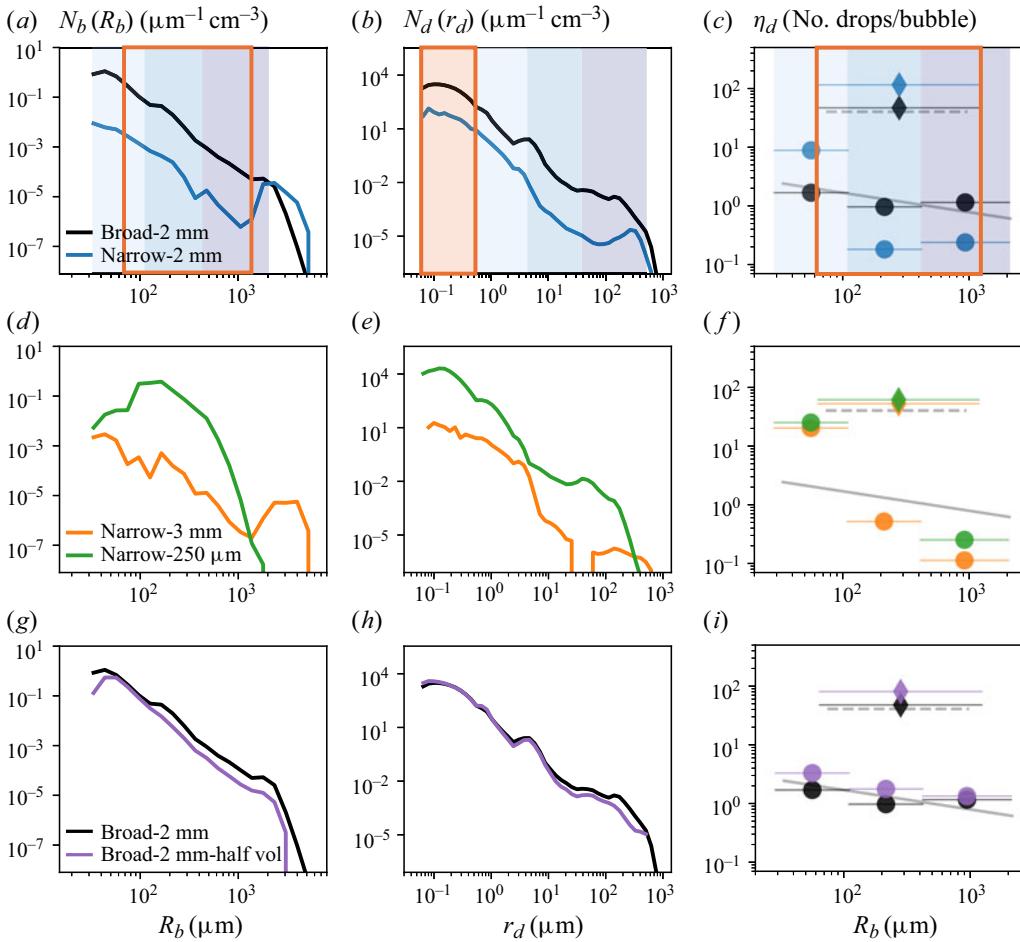
Figure 6. Size distributions of bursting bubbles, $N_b(R_b)$ (*a,d,g*), and drops, $N_d(r_d)$ (*b,e,h*), in terms of the liquid drop radius, r_d, for various case comparisons. The bubble size distributions presented vary significantly, including broad-banded cases and three narrow-banded cases peaking at radii of 2 mm, 3 mm and 250 μm, with a corresponding variety of drop size distributions. To calculate the drop production efficiency presented in the rightmost column (*c,f,i*), the bubble and drop size distributions are first integrated in the shaded or outlined size buckets, where the link between the bubble and drop sizes approximates the link suggested by scaling laws for individual bubble bursting. The resulting number of drops in each size range is then divided by the number of bubbles in the corresponding shaded size range (outlined for the film flap range) to obtain an average number of drops produced per bubble in each bubble size bucket (production efficiency η_d, shown as circles within the jet drop size range corresponding to the blue shaded regions and diamonds for the assumed film flap drop size range corresponding to the orange boxes). Shaded grey lines show the number of drops per bubble predicted by the individual bubble bursting scalings for jet (solid line) and film flapping (dotted line) production mechanisms (tested in § 4.2; see table 3 for details). Cases shown are (*a–c*) narrow-2 mm versus broad-2 mm, (*d–f*) narrow-3 mm versus narrow-250 μm and (*g–i*) broad-2 mm versus broad-2 mm-half volume. Further details of each case are found in table 1, and the uncertainty associated with the production efficiency values shown in (*c,f,i*) is discussed in Appendix B.

4.1. *Direct attribution between measured bubbles and drops*

We first show the drop size distributions resulting from various bubble size distributions and discuss how different sizes of drops may be attributed to different sizes of bursting bubbles. Figure 6 shows the size distributions of bursting bubbles, $N_b(R_b)$ (*a,d,g*), and

drops, $N_d(r_d)$ (*b,e,h*), as well as the ratio of the number of drops produced per bubble η_d (*c,f,i*), in chosen size ranges.

Figure 6(*a–c*) shows the two sample cases described in § 2.2.4 (figures 4 and 5, narrow- and broad-2 mm injection cases). Both cases use the same needles and flow rate, but in the broad case turbulent flow is created underwater. As described above, turbulence induces bubble breakup and creates a broad-banded bubble size distribution with a continuum of bubbles spanning radii of 30 μm to almost 5 mm. Without turbulence, the distribution has a peak around $R_b = 2$ mm with a lower number of smaller bubbles. The two cases (broad- and narrow-banded) have a relatively comparable number of bubbles around 2 mm, near the needle injection size. For the submillimetric bubbles, there is a large difference of about two orders of magnitude in the number of bubbles (because without turbulence, the only small bubbles present are formed by pinch-off at the needles, see § 2). Moving to the drop size distribution, we observe a corresponding difference of similar magnitude between the drop size distributions for nearly the entire range of sizes measured in the experiment, until the number of drops becomes more comparable between cases for $r_d > 400$ μm. This suggests that the drops we measure below radius 400 μm are produced by bubbles with radii smaller than approximately 2 mm (shaded in colour).

We therefore focus on the submillimetric portion of the bubble size distribution (shaded in colour) and consider the link between the measured submillimetric bubbles and produced drops. We first test a direct attribution of drops to bubbles, dividing the number of measured drops by the number of measured bubbles in discrete size bins (shaded/outlined with the corresponding colours).

Size buckets are chosen to approximate the individual bubble size scaling laws for jet and film flapping production mechanisms (discussed in more detail in § 4.2 and Berny *et al.* 2021; Deike *et al.* 2022; Jiang *et al.* 2022). The corresponding bubble and drop ranges are shown in shaded/outlined colours in figure 6, where the overlap in bubble sizes represents the fact that bubbles can produce both jet and film flap drops in parallel processes. For the film flap scaling, we test the link between bubbles of radii $R_b = [70, 1200]$ μm and drops of radii $r_d < 0.5$ μm (outlined/shaded in orange). For the jet drop scaling, we consider the ability of bubbles in the range $R_b = [30, 2000]$ μm to produce drops of $r_d > 0.5$ μm (shaded in blue). The total regions tested for jet drop production are approximately evenly divided into three smaller log-spaced size buckets for both bubbles and drops, and the buckets are linked in size order.

The distributions are then integrated within each assigned size bucket to calculate a total number of bubbles or drops (per measurement volume) within that size range, given by $\rho_b = \int_{R_{b1}}^{R_{b2}} N_b(R_b)\, dR_b$ for bubbles within the size range $[R_{b1}, R_{b2}]$ and $\rho_d = \int_{r_{d1}}^{r_{d2}} N_d(r_d)\, dr_d$ for drops in the size range $[r_{d1}, r_{d2}]$. By dividing the number of drops in a size bucket by the number of bubbles in the corresponding size bucket, we calculate a drop production efficiency (the number of drops produced per bubble) for each pair of size buckets, defined as $\eta_d = \rho_d/\rho_b$.

Resulting drop production efficiencies are shown in the right column of figure 6(*c,f,i*), calculated from the shaded ranges (jet drop, circles) or outlined ranges (film flap drop, diamonds) of bubble and drop size buckets for the two cases. Note that the values of the efficiencies would shift somewhat if we chose to split the drop size distribution at a value other than $r_d = 0.5$ μm when testing the attribution to the assumed bubble size ranges. The cutoff radius at $r_d = 0.5$ μm was chosen because it falls between the largest predicted film drop and smallest predicted jet drop for the range of bubble sizes present in the experiment.

For the broad-banded case in figure 6(*c*), we observe approximately 50 drops/bubble in the assumed film flap range (black diamond) and approximately $1.0-1.8$ drops/bubble

Mechanism	$[R_{b1}, R_{b2}]$ (μm)	$\langle r_d \rangle (R_b)$ (μm)	$n_d(R_b)$	Order of Γ Distribution
Film flap	[70, 1000]	$0.40\,(R_b/l_c)^{1/3}$	40	4
—	—	[0.1, 0.3] μm	—	—
Jet (G-C)	[30, 2300]	$0.60\,l_\mu\,(\sqrt{La}(\sqrt{(La/La_*)} - 1))^{5/4}$	$30\,(R_b/l_\mu)^{-1/3}$	11
—	—	[1, 400] μm	[3, 0.6]	—
Jet (B-R)	[30, 500]	$0.20\,R_b(1 - (0.033^2 R_b/l_\mu)^{-1/4})$	$30\,(R_b/l_\mu)^{-1/3}$	11
Film centrifuge	[900, 10 000]	$0.25\,R_b^{3/8}\,h_b^{5/8}$	$0.040\,(R_b/l_c)^2 (R_b/h_b)^{7/8}$	11
—	—	[1, 50] μm	[10, 120]	—

Table 3. Equations and parameters used to calculate the drop size distribution $N_d(r_d)$ from input bubble size distribution $N_b(R_b)$, following (with adaptation) the scaling laws developed for individual bubble bursting. Equations used for the mean size $\langle r_d \rangle (R_b)$ and number $n_d(R_b)$ of emitted drops are shown, as well as the radius bounds $[R_{b1}, R_{b2}]$ and the order of the gamma distribution (assumed to represent the distribution of drop sizes $p(r_d/\langle r_d \rangle, R_b)$) required to compute $N_d(r_d)$ as described in (4.1). Film flap: size scaling based on the data from Jiang *et al.* (2022), discussed in Deike *et al.* (2022). The drop number is taken as a single value of 40 drops/bubble, based on Jiang *et al.* (2022). Jet (G-C)/Jet (B-R): uses the formulation for the first drop size given by Gañán-Calvo (2017) and Blanco–Rodríguez & Gordillo (2020), respectively. The drop number scaling from Berny *et al.* (2021) is used with a modified prefactor suggested by Wang *et al.* (2017). The Laplace number $La = R_b/l_\mu$ controls jet drop ejection, comparing the radius of the bursting bubble, R_b, to the visco-capillary length, $l_\mu = \mu^2/\rho\gamma$, using the values for physical parameters given in § 2.1. Here $La_* = 550$ is taken for the critical Laplace number for jet drop formation in the G-C formulation (Walls *et al.* 2015; Berny *et al.* 2020). Note that the B-R expression provided here is valid for $Bo = \rho g R_b^2/\gamma \leq 0.05$ and $La > 1111$, which corresponds here to bubbles in the radius range $R_b = [20, 500]\,\mu$m, so this formulation is applied only to our measured bubbles of radii smaller than 500 μm. The G-C scaling is applied to bubbles of radii larger than 30 μm and would diverge for smaller radii between $10-20\,\mu$m. Film centrifuge: scalings developed by Lhuissier & Villermaux (2012), with size and number of drops determined by the bubble size and film thickness h_b, where h_b scales with R_b^2/l_c and spans [0.2, 30] μm for bubbles with $R_b > 0.4l_c$ (capillary length $l_c = \sqrt{\gamma/\rho g} = 2.3$ mm for the artificial seawater solution). Sensitivity of the predicted drop size distributions to different choices of R_{b1}, R_{b2} and the order of the gamma distribution are discussed in Appendix B.

across the jet drop size buckets (black circles). For the narrow-banded case, we observe a high efficiency of around 100 drops/bubble in the film flap size range (blue diamond), while the small jet drop efficiency is around 9 and the larger jet drop efficiency is below unity (blue circles).

These numbers can be compared with the efficiencies discussed in the literature. The light grey lines in the same plot represent the drop number given by the individual bubble bursting scaling laws used throughout the paper for jet drops (solid, between $0.6-3$ drops produced per bubble (Wang *et al.* 2017)) and film flap drops (dotted, 40 drops per bubble (Jiang *et al.* 2022)). Detailed equations for the scalings shown here, based on past work in the literature, are provided in table 3 and described in § 4.2. Comparing the calculated efficiencies for the two sample cases to the approximate individual bursting scaling laws, we see reasonable agreement for the broad-banded case. For the nearly monodisperse case, significant differences are observed and various interpretations can be proposed. The higher efficiency of film flap drops could be related to the proposed bubble pinch-off effect/small aerosol formation in the bulk discussed in the recent work of Jiang *et al.* (2024), with this effect potentially smeared out or not occurring in the presence of turbulence (note that, for the narrow-2 mm case, high-speed movies confirm collisions at the needle tip/during bubble pinch-off as discussed in Jiang *et al.* (2024);

these collisions at the needle tips are not observed in the narrow-3 mm case). The higher jet drop efficiency for the small bubbles, which closely match direct numerical simulations for similar conditions (Berny *et al.* 2021), could be due to the fact that either the low surface density of bubbles or a calmer free surface are necessary to obtain such efficiency. Larger jet drop low production efficiency might be related to a lack of statistical convergence in measuring these drops with the holographic system. Sources of uncertainty involved in the calculation of the production efficiency values presented in figure 6 are discussed in Appendix B.

To further probe the link between collective bursting bubbles and ejected drops, we perform the same direct attribution analysis for several initial bubble configurations and analyse the corresponding change in the drop size distribution and associated uncertainties. We look next at figure 6(*d–f*) to analyse how injecting bubbles larger or smaller than 2 mm, with a nearly monodisperse size distribution, affects the drop production. For the injection of larger bubbles (panel *d*), the peak of the size distribution is closer to a radius of approximately 3.5 mm (compared with the previous case of approximately 2.3 mm bubbles). The small bubble case features a wider peak of primarily submillimetric bubbles centered near 250 μm (see details in table 1 and surface images in figure 1).

From the size distributions, it is immediately evident that many more submicron droplets are produced (figure 6*e*) when more small submillimetric bubbles are present (figure 6*d*). We observe an approximately 3 order-of-magnitude difference between the size distributions of the small bubble case and the large bubble case, where very few submicron drops are produced. As shown by the large bubble case, when we measure very few submillimetric bubbles, we measure very few submicron drops. This demonstrates that bubbles predominantly larger than 2 mm do not produce a significant amount of submicron aerosols in this configuration.

Comparing to individual bursting scalings, in figure 6(*f*) we see a reasonable efficiency of approximately 60 drops/bubble for both cases for the proposed film flap range (green and orange diamonds). For the two largest jet drop bins in figure 6(*f*), the efficiencies for bubbles are low (green and orange circles; efficiencies below 0.1 associated with a very small number of drops are not shown on the plot), with similar values to those discussed above for the 2 mm narrow-banded case (figure 6*c*, blue circles). For the smallest jet drop bin, the efficiencies are high, at around 20 drops/bubble. We note that the overall efficiencies are consistent across all the cases despite the large differences in the bubble size distributions (see the plot of the number of drops versus the number of bubbles in Appendix A), and it is only once we assume a link between the bubbles sizes and drop sizes for this attribution that differences in efficiencies appear for the narrow-banded cases compared with the broad-banded cases. The different efficiency values found in the narrow-banded cases imply that some subtleties of the bubble–drop link may be blurred across neighbouring size buckets for the continuum of bubble and drop sizes present in the broad-banded cases, which seem to match the single bubble scaling laws well.

The lack of large drops for two of the narrow-banded cases (peaking at radii of 2 mm and 3 mm) can be explained by either missing drops due to the small field of view or by a physical collective effect where neighbours may somehow limit production efficiency in these nearly monodisperse conditions. To take a step in investigating a potential collective effect that may modulate the bubble to drop size link or affect overall production efficiencies, we look at the broad-banded cases and compare cases with 32 versus 16 bubbling needles ('broad-2 mm' and 'broad-2 mm-half volume' – the cases have the same flow rate per needle, so we effectively halve the injected volume of bubbles). Aside from decreasing the injected volume, decreasing the number of needles allows the bubbles to arrive at the surface spaced apart from each other, so that most bubbles burst individually

instead of clustered, as visualised in figure 1(*f*). Looking at the size distributions for these two cases, shown in figure 6(*g–i*), we observe that a smaller number of bursting bubbles (panel *g*) results in a drop size distribution that is very similar to that of the clustered case, especially for the submicron drops (panel *h*). Looking at the efficiencies (panel *i*), the 16 needle case has a higher efficiency than the 32 needle case across all bubble sizes, indicating that a collective effect could potentially be limiting the drop production efficiency.

Through the attribution of measured drops to measured bubbles analysed in this section, we have observed that the broad-banded cases show an overall agreement between our calculated bursting efficiencies and those found from the single bubble scaling laws for film flap and jet drop production, with a possible reduction of efficiency for the collective bursting (figure 6*g–i*). The narrow-banded cases demonstrate that submicron drops are produced by bubbles with radii smaller than approximately 1 mm (figure 6*d–f*), and that nearly monodisperse clusters may display a reduced efficiency in jetting for bubbles with radii above approximately 100 μm and an increased efficiency for the smaller bubbles (figure 6*c,f*).

4.2. *Using individual bubble scaling laws to predict drops produced by measured bubbles*

Now we investigate the distributions of drops predicted by the individual bubble bursting scaling laws – which provide the number and size of drops for a given bubble – combined with the measured bubble size distributions, and we then compare the predicted drop size distributions to our measured drop size distributions. We use the results to further evaluate how well the individual bursting relations describe collective bursting results across all cases. To predict the drops produced by the collection of bursting bubbles, we consider the approach from Lhuissier & Villermaux (2012), initially proposed for production of film drops via a centrifuge mechanism and extended to jet drops (Berny *et al.* 2021) and film flap drops (Deike *et al.* 2022). For a specific drop production process, the total drop size distribution $N_d(r_d)$ produced by an ensemble of bubbles is obtained by integrating individual bursting scalings over the size distribution of bursting bubbles $N_b(R_b)$ in the size range $[R_{b1}, R_{b2}]$:

$$N_d(r_d) = \int_{R_{b1}}^{R_{b2}} \frac{N_b(R_b)n_d(R_b)}{\langle r_d \rangle(R_b)} p\left(\frac{r_d}{\langle r_d \rangle}, R_b\right) \, \mathrm{d}R_b. \tag{4.1}$$

Here $N_b(R_b)$ is the measured bubble bursting size distribution, $\langle r_d \rangle(R_b)$ is the mean drop size produced by a bursting bubble of size R_b, $n_d(R_b)$ is the number of drops produced by a bubble bursting of size R_b, and $p(r_d/\langle r_d \rangle, R_b)$ is the probability density function of drop sizes produced by a bubble of size R_b, assumed to be a gamma distribution of known order (Lhuissier & Villermaux 2012; Berny *et al.* 2021; Deike *et al.* 2022). Sensitivity of the resulting drop size distributions to the order of the gamma distribution and to the chosen radius bounds (R_{b1} and R_{b2}) are discussed in Appendix B.

We perform the integration, using the measured bubble size distribution, for each individual drop production mechanism, as summarised in table 3. Scalings for the number and size of drops produced by the bursting of single bubbles have been developed for three main modes of drop production: film centrifuge, film flap and jet drop production. The integration for each mechanism over many bubble sizes is similar to the analysis performed by Deike *et al.* (2022) (using assumed/modelled bubble size distributions) and Néel *et al.* (2022) (measuring only larger scales of drops and bubbles), as well as for individual mechanisms in Lhuissier & Villermaux (2012) (film centrifuge drops, assumed/modelled
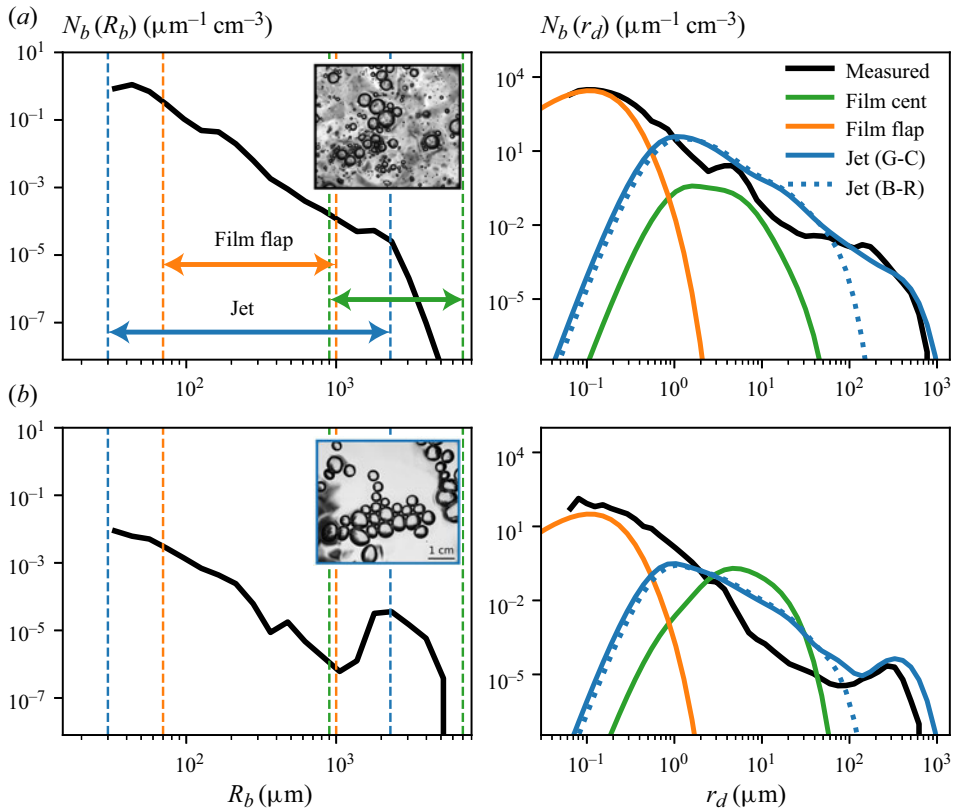
Figure 7. Measured bubble ($N_b(R_b)$) and liquid drop ($N_d(r_d)$) size distributions for the 2 mm injected bubble cases with (*a*) broad-banded and (*b*) narrow-banded distributions. Overlaid coloured lines represent the predicted drop size distribution from each production mechanism for individual bubble bursting (see details in table 3), integrated over many bubble sizes using the measured bubble size distribution. Bubble size ranges used in the integration for each mechanism are labelled in the same colour on the measured bubble size distributions. Note that the jet formulation from Blanco–Rodriguez & Gordillo (2020) (B-R) is only applied in the range $R_b = [30, 500]\,\mu\text{m}$.

bubble size distribution), Blanco–Rodríguez & Gordillo (2020) (jet drops), and Gañán-Calvo (2023) (extended jet drops using assumed/modelled bubble size distributions).

Figure 7 shows the result of the integration in (4.1) for each production mechanism, compared with the measured drop size distribution for the 2 mm bubble size cases (broad-banded and narrow-banded). The scalings and coefficients used for each drop production mechanism are given in table 3 and depicted graphically in figure 6.

From figure 7, we can discuss how well scaling laws for each drop production mechanism describe the experimental drop size distribution, beginning with the broad-banded case presented in the top row.

We start with jet drop production, where drops are created by fragmentation of the jet formed by the focusing of capillary waves into the collapsed bubble cavity. For bubbles of sizes between 30 μm and the capillary length ($l_c \sim 2.3$ mm for the artificial seawater solution), which are able to produce jet drops (Walls *et al.* 2015; Berny *et al.* 2020), we apply the theoretical formulation developed by Gañán-Calvo (2017) for the resulting drop size. Because there is no theoretical prediction for the number of jet drops produced by the bursting bubble, we consider the scaling proposed by Berny *et al.* (2021) for the number of drops (coherent with experimental data from Spiel 1997*b*; Ghabache *et al.* 2014; Ghabache

& Séon 2016) with a modified prefactor. The modified prefactor means that bubbles of radii $R_b = [30, 2300]\,\mu$m are predicted to produce $n_d = [3, 0.6]$ jet drops per bubble, which is lower than the $n_d = [11, 3]$ drops from the Berny *et al.* (2021) fit to various data for individual bubble bursting, but is in agreement with the collective bursting experiment from Wang *et al.* (2017) (see figure 1 from their paper).

For the broad-banded case, shown in figure 7(*a*) (bubbles on the left, drops on the right), the jet drop scaling laws (blue lines) match the measured drop size distribution (in black) very well for drops of radii approximately 1 to $500\,\mu$m. Because the magnitude of the distributions lines up well using the $0.6−3$ jet drops produced per bubble across the radius range (where smaller bubbles produce more drops), the average number of jet drops produced by many collective bursting events is likely lower than the $3−11$ drops that a single bubble is physically able to produce (across the same radius range). Each bursting event is not necessarily as efficient as every other event. In the collective bursting set-up, some bubbles may be disturbed by the rising or bursting of their neighbours or by water fluctuations that could affect the cavity collapse and jet formation, which would reduce the overall drop production efficiency. The jet drop size formulation developed in Blanco–Rodríguez & Gordillo (2020), based on capillary wave selection, was also tested (blue dotted line). Since it yields very similar results over the range of bubble radii we measure where the scaling is valid (as the drop sizes as a function of bubble sizes were derived using the same experimental and numerical data in both formulations), we use the equation from Gañán-Calvo (2017) for the rest of the analysis.

Next we consider the mode of film drop production proposed in Jiang *et al.* (2022), where they report submicron drops produced by bursting bubbles in the approximate radius range $R_b = [70, 1000]\,\mu$m, which they attribute to a film flapping mechanism. As shown in figure 7, the size scaling and order of magnitude associated with the film flap drops (orange) match well with the measured distribution (black) for the broad-banded case.

Finally, for film drop production through a centrifuge mechanism, Lhuissier & Villermaux (2012) describe the fragmentation of ligaments formed as the cap of a bubble with radius $R_b > 0.4l_c$ retracts. We observe that the predicted distribution (green) does not describe the data well, falling below the measured distribution for the broad-banded case. The film centrifuge scaling leads to significantly fewer drops than the jet drop counterpart (in the size range where both mechanisms are applicable) due to the fact that there are fewer larger bubbles (above the capillary length) where the centrifuge mechanism is effective. Note that the film centrifuge scaling does not predict submicron drops.

Looking now at the narrow-banded case presented in figure 6(*b*), we observe that the film flap results again match the peak and magnitude relatively well (orange line), only slightly below the experimental data (black line). The jet scalings (blue) approximate the correct drop magnitude at their peak, around $1\,\mu$m, but overpredict some larger drops. While this overprediction could be related to limits in measuring larger drops in the experiment, we also note that if a truncated gamma distribution is used, such that $p(r_d/\langle r_d \rangle, R_b) = 0$ for bubbles of radii $R_b > 2$ mm, the resulting predicted drop size distribution describes the large drops well (shown in Appendix B for the broad-2 mm and narrow-2 mm cases). The film centrifuge mechanism again does not describe the data, this time overpredicting the number of drops. This significant overprediction may be related to fact that the centrifuge mechanism can frequently eject drops horizontally, reducing their measured efficiency as these drops likely fall back to the water without being transported upwards into the measurement region (Néel & Deike 2022; Shaw & Deike 2024).

From the two sample cases, we find that the experimental drop size distributions can be predicted well from knowledge of the experimental bubble size distribution using scaling laws for film flap drop and jet drop production for individual bubble bursting,
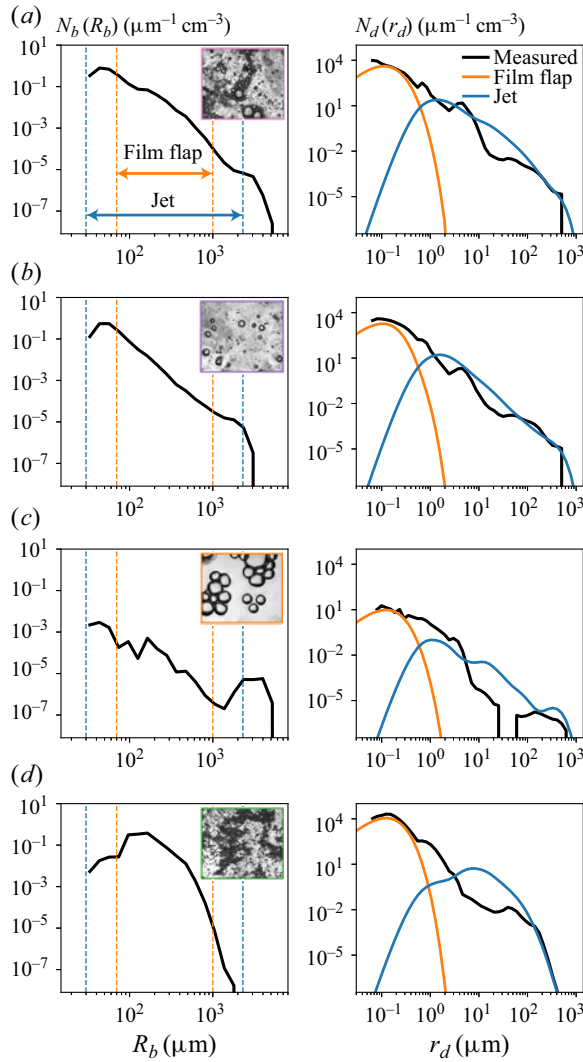
Figure 8. Bursting bubble ($N_b(R_b)$) and liquid drop ($N_d(r_d)$) size distributions for the cases: (*a*) broad-3 mm, (*b*) broad-2 mm-half volume, (*c*) narrow-3 mm and (*d*) narrow-250 μm, with representative surface images inlaid for each case. The predicted drop size distributions from individual bubble bursting scaling laws are plotted in colour for film flapping (orange) and jet (blue) drop production (see details in table 3), with the bounds of the associated portions of the bubble size distribution shown with dashed lines of the same colour.

with some differences between data and model for jet drops above $r_d = 10$ μm. The film centrifuge mechanism does not appear to be statistically relevant and is ignored in the rest of the analysis. In the next section we explore how well this framework describes spray generation for the other bubble size distributions.

4.3. *Jet and film drop individual bubble bursting scaling laws for all cases*

Figure 8 compares the measured and predicted drop size distributions for the remaining cases, using the same set of parameters described in table 3. As introduced in the previous section, the individual bubble scaling laws match the data very well for the broad-banded cases, shown in figure 8(*a*) (bubbles on the left, drops on the right) for bubbles of original

injection size 3 mm, which are again characterised by a continuum of bubble sizes after breakup in turbulence. The magnitude of the distributions again match well with the data (black) using the $0.6-3$ drop per bubble assumption for the jet drops (blue), as discussed in the previous section, and the film flap (orange) magnitude also lines up well with the data. In this case, the framework works well across all scales with the two modes of production – with the jet drop mechanism dominating drop production above $1\,\mu m$ and the proposed film flap mechanism producing submicron drops.

Figure 8(*b*) shows the distributions for the case with 16 bubbling needles, where bubbles are spaced out on the surface and burst individually. While the jet drop scaling still matches well, the film flap prediction seems to miss some measured drops. The slight underprediction for this case – compared with the better match for submicron drops in figure 7(*a*) – may indicate a higher efficiency for the individual bursting case due to a potential collective effect limiting drop production. For the cases with narrower distributions, shown in figure 8(*c,d*), the measured and predicted distributions match well in the size range of film flap drops but are less coherent for the region described by jet drop production. In the large bubble case (panel *c*), again fewer large jet drops are measured than predicted. For the small bubbles, the prediction overestimates drops around radius $r_d = 10\,\mu m$. As discussed in § 4.1 for the direct attribution, the narrow-banded cases reveal that the assumed size link between bubbles and drops is not entirely accurate in this collective bursting set-up when large aggregates of bubbles of nearly the same size are present. Indeed, it seems that the predicted jet drop distribution for the cases in figure 8(*c,d*) may be missing some drops below radius $r_d = 1\,\mu m$, which can be seen from the gap between the predicted and measured distributions where the film and jet curves overlap. Néel & Deike (2021) and Néel *et al.* (2022) observed a similar shift/broadening in the peak size of ejected drops for collective bursting of millimetric bubbles in surfactant solutions of various concentrations, which remains unexplained. These inconsistencies may be explained by a surfactant or collective effect and require further investigation. We note also that the predicted jet drop production is sensitive to the chosen critical Laplace number (La^*, the drop ejection threshold), shifting the predicted drop size distribution to somewhat smaller sizes if this value is increased.

Overall, the drop size distribution produced by clustered bursting bubbles in artificial seawater can be reasonably well described from knowledge of the bubble size distribution, especially for the broad-banded distributions. By integrating individual bubble bursting scaling laws for size, number and distribution of ejected drops for all measured bubble sizes, we arrive at a reasonable estimate of the drop size distribution. Further study is required to explain the details of deviations in large jet drop production and spray generation by denser rafts of small bubbles, and to more precisely connect the two production mechanisms around their respective cutoffs around $1\,\mu m$ (large size for film drops and small size for jet drops), with possible collective effects.

5. Conclusion

In this paper, we have characterised drop production by collective bubble bursting using a steady-state bubbling tank set-up. Systematic measurements of bulk bubbles, surface bubbles and drops/salt aerosols from many combined techniques allowed us to measure bubble radii spanning $30-5000\,\mu m$ and drop radii spanning $0.05-500\,\mu m$, covering five total orders of magnitude that correspond to realistic ocean scales for drop production by bursting of bubbles generated by breaking waves. We used the complete measured size distributions to analyse the physical link between bubbles and drops for a variety of cases with different bulk bubble size distributions, both by directly attributing measured drops

to measured bubbles and by applying scaling laws for individual bubble bursting to predict the drop size distributions from the measured bubble size distributions.

By analysing collective bubble bursting for a variety of bulk bubble size distributions in the experimental set-up presented in this paper, we have observed the following results.

(i) Bulk and surface bubbles can be reasonably linked through a simple flux idea assuming a bulk bubble rise velocity parameterisation and constant surface bubble lifetime, and coalescence is not a dominant effect to consider with artificial seawater (figure 5).

(ii) Bursting bubbles with radii greater than approximately 1 mm do not produce significant numbers of submicron drops (shown most clearly in figure 6*a*–*f*).

(iii) A modest collective effect (around a factor 2) may decrease the production efficiency of clustered bubbles compared with individual bubble bursting (figure 6*g*–*i*).

(iv) Scaling laws developed for individual bubble bursting can describe the measured drop size distribution well for broad-banded bulk bubble size distributions characterised by a continuum of both bubble and ejected drop sizes (figures 7*a* and 8*a*,*b*). Drops predicted by the proposed film flapping mechanism for bubbles of radii $70-1000\,\mu m$ describe the submicron portion of the drop size distribution with an efficiency of about 40 drops per bubbles. Drops above approximately $1\,\mu m$ can be explained following scaling laws for jet drops with an efficiency for the number of drops produced by bubbles of radii $30-2300\,\mu m$ between $3-0.6$ jet drops per bubble.

(v) Cases with a narrower size range of bulk bubbles were not described as well by the single bubble scalings. Jet drop scalings primarily overpredicted the production of large drops (and displayed a shift in size) compared with the experimental measurements. This discrepancy remains unexplained but suggests the possibility of a collective effect – when clusters of bubbles of similar sizes burst – that may modify bursting efficiency or the link between sizes of bubbles and ejected drops (figures 7*b* and 8*c*,*d*).

Overall, we have studied the link between bulk bubbles, surface bubbles and drops in a collective bursting set-up, and we have experimentally confirmed the applicability of mechanistic ocean spray emission functions based on individual bursting mechanisms (Deike 2022; Deike *et al.* 2022). We have leveraged many combined measurements and cases of diverse bubble size distributions and underwater conditions to analyse the attribution of drops to bursting bubbles. The potential collective effect suggested by these experiments will be studied further through dynamical measurements of bursting in bubble rafts. Future work using the same set-up will explore how the link between bursting bubbles and emitted drops changes for solutions of different surfactant and temperatures, further extending the applicability of physics-based sea spray emission functions (Deike *et al.* 2022) to open ocean conditions in the presence of biological activity (Burrows *et al.* 2014) and taking steps to understand sea spray emissions by bubble bursting in other increasingly realistic configurations for ocean conditions.

Declaration of interests. The authors report no conflict of interest.

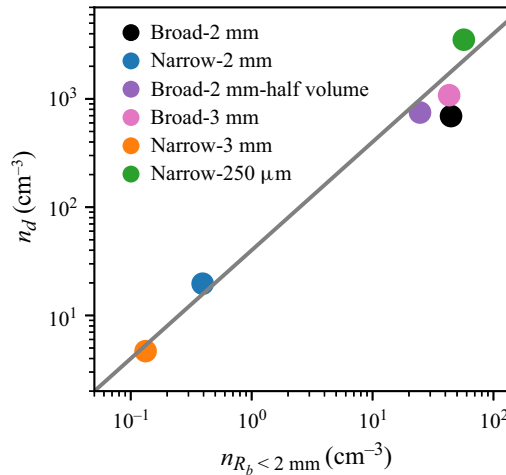**Data availability statement.** Data used to prepare this work is publicly available at https://doi.org/10.34770/7s70-0v84.

Figure 9. Total number of drops (n_d) versus the number of bubbles with radii below 2 mm ($n_{R_b < 2\,\text{mm}}$), both per unit volume, for each case explored in the paper. The grey line represents $n_d = 40\ n_{R_b < 2\,\text{mm}}$, where the coefficient represents an average drop production efficiency, assuming drop production by bubbles with $R_b < 2$ mm.

Appendix A. Average drop production efficiencies

The different conditions explored throughout the paper are characterised by very different numbers of bubbles at the surface, and therefore, very different numbers of emitted drops, as illustrated by figure 9, showing the number of drops as a function of the number of bubbles with radii smaller than 2 mm. As indicated in the figure and already mentioned, the number of bubbles found in our experiments span around three orders of magnitude. An averaged drop production efficiency for each surface bubble configuration can be evaluated by an approximate linear relationship between the number of drops and the number of bubbles, as indicated by the solid line in figure 9. This linear fit suggests similar average efficiencies among all cases, with about 40 drops per bursting bubble. We also observe that the two cases of broad-banded bubble size distributions with significant clustering (the broad-2 mm and broad-3 mm cases) show a reduced efficiency (pink and black symbols being below the linear trend).

Experiments were also performed for various air flow rates of 200, 400 and 800 cm^{3}min^{-1} for the bubbler configuration, and all cases yield drop production efficiencies similar to those reported in figure 9, with no significant measurable effect of the air flow rate on the production of small drops in our set-up.

Appendix B. Uncertainty in drop production efficiencies and sensitivity of predicted drop size distributions

When performing the direct attribution of drops to bubbles from the data (§ 4.1) and calculating drop production efficiency for film and jet drops, there are uncertainties in the measurement of the bubble size distribution and drop size distribution as well as uncertainties related to the chosen radius bounds of integration. As discussed in the experimental methods, the experimental size distributions are statistically converged and the statistics are highly reproducible when repeating the same experiment. From measurements of bubble and drop size distributions, the estimated uncertainty on the efficiency values shown in figure 6 is around a factor 2.
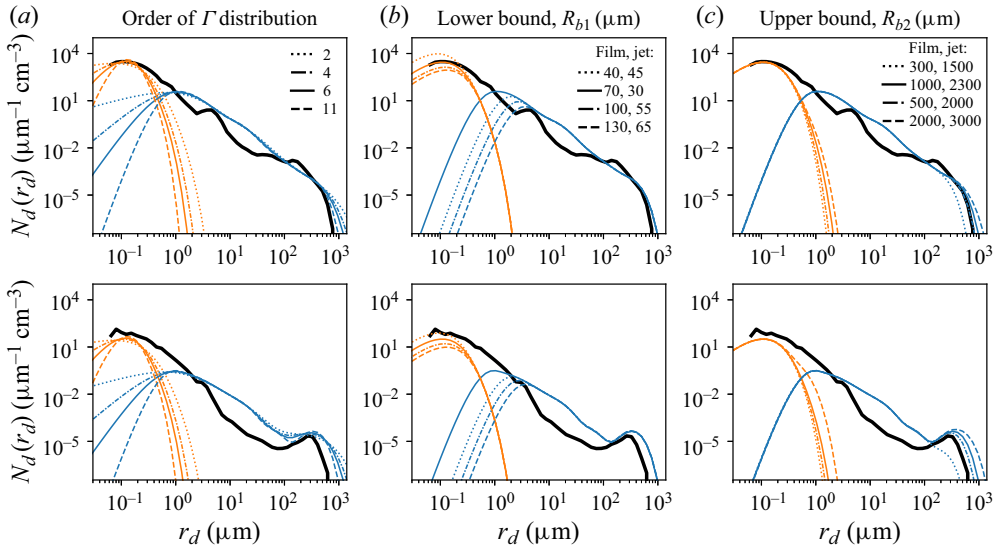
Figure 10. Bursting bubble ($N_b(R_b)$) and drop ($N_d(r_d)$) size distributions for the broad-2 mm (top row) and narrow-2 mm (bottom row) cases. The predicted drop size distributions from individual bubble bursting scaling laws are plotted in colour for film flapping (orange) and jet (blue, from G-C scaling) drop production. The sensitivity of the predicted drop size distributions to parameters of the model/integration (see (4.1)) is shown for (a) the order of the gamma distribution $p(r_d/\langle r_d \rangle, R_b)$ (varied between 2 and 11), (b) the lower bound, R_{b1}, for the selected radius range (varied between 40 and 130 μm for film flapping and between 30 and 65 μm for jet drop production) and (c) the upper bound, R_{b2}, for the selected radius range (varied between 300 and 2000 μm for film flapping and between 1500 and 3000 μm for jet drop production). For the lower and upper bounds, the solid line represents the distributions/set of parameters used in figure 7. Parameters are described further in table 3.

We note, however, that the predicted drop size distributions shown in §§ 4.2 and 4.3 (or the figure 6 efficiencies calculated in a particular size bucket) can be quite sensitive to the choice of bubble and/or drop radius ranges that are integrated for each drop production mechanism (film or jet). To calculate the efficiencies presented in figure 6, the total ranges of assumed jet drops and corresponding bubbles are split into approximately equal log-spaced buckets, of proportional sizes between the drop and bubbles. Shrinking/expanding/shifting these buckets will cause the efficiency values to shift up or down slightly, which could change the physical interpretation. The interpretation we propose results from our understanding of individual bursting processes discussed in the literature and from the consistency between the message of the direct attribution (§ 4.1) and the drop size distributions predicted by the individual bubble bursting scaling laws combined with the measured bubble size distributions (§§ 4.2 and 4.3). We note that the overall average drop production efficiencies (see Appendix A) are relatively constant across all cases. This overall efficiency is dominated by small drop production by bubbles of intermediate size, which is shown in both our methods of drop attribution to bursting bubbles for all cases, and gives confidence in our chosen interpretation.

Regarding the analysis presented in §§ 4.2 and 4.3, we provide further details on the sensitivity of the drop size distributions predicted using the single bubble scalings (used to generate the coloured curves presented in figures 7 and 8), shown in figure 10. We test the sensitivity to the order of the gamma distribution representing $p(r_d/\langle r_d \rangle, R_b)$ (panel a) and to the lower (panel b) and upper (panel c) radius bounds chosen for the film flapping and jet drop production mechanisms. From these figures, we observe that the order of
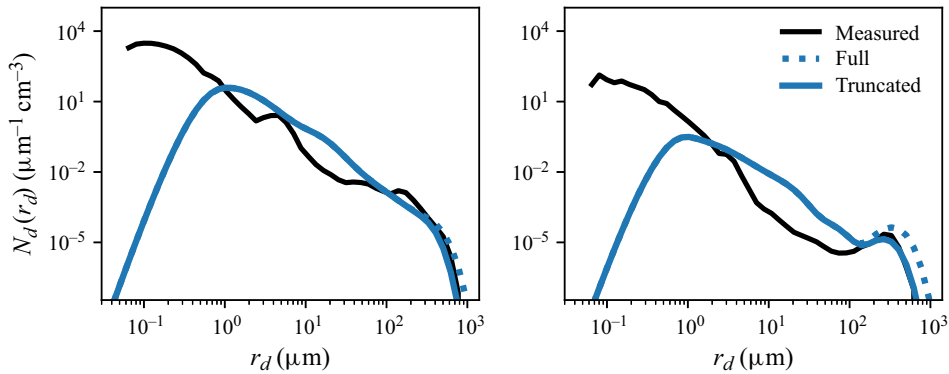
Figure 11. Measured and predicted drop size distributions ($N_d(r_d)$) for the broad-2 mm (left) and narrow-2 mm (right) cases. The predicted jet drop size distributions are computed using the full gamma distribution for all bubble radii (dotted line, also shown in figure 7) and the truncated gamma distribution (solid line). The truncated gamma distribution is equal to zero for bubbles of $R_b > 2$ mm.

the gamma distribution primarily affects the shape of the curve at the small drop size cutoff, and the chosen upper radius bound shifts the large drop size cutoff. The predicted distributions are much more sensitive to the chosen lower radius bound for each production mechanism, which more significantly affects the magnitude of the predicted distributions for the film flap drops and is critical in defining the location of the peak for small jet drops (and, therefore, also the important overlap between film flap and jet scalings).

We note that we use the gamma distribution to represent the statistics of drops emitted by a single bubble bursting, however, another type of distribution, such as a lognormal distribution, could be used. As discussed in Berny *et al.* (2021), when integrating over a wide range of bubbles sizes, the scaling for the mean size and number of drops emitted dominates over the type of function used, and the type of function will mostly modulate the result near the bounds of integration. The gamma distribution has the practical advantage of allowing for analytical integration when considering bubble size distributions represented as power laws, as discussed in Lhuissier & Villermaux (2012).

Regarding the larger drop sizes, we can also consider using a truncated gamma distribution in the integration. In this case, the distribution of drop sizes produced by an individual bursting bubble ($p(r_d/\langle r_d \rangle, R_b)$) would be represented by the gamma distribution for bubbles smaller than a chosen cutoff radius R_b^{max}, and equal to zero for bubbles larger than this cutoff size. Figure 11 shows the comparison between jet drop size distributions computed using the full gamma distribution and the truncated version, which is set to zero for bubbles larger than the chosen cutoff radius of $R_b^{max} = 2$ mm. Using this truncated gamma distribution, the predicted drop size distributions describe the data for the large drop sizes very well.

REFERENCES

BERNY, A., DEIKE, L., SÉON, T. & POPINET, S. 2020 Role of all jet drops in mass transfer from bursting bubbles. *Phys. Rev. Fluids* **5** (3), 033605.

BERNY, A., POPINET, S., SÉON, T. & DEIKE, L. 2021 Statistics of jet drop production. *Geophys. Res. Lett.* **48** (10), e2021GL092919.

BLANCHARD, D.C. & SYZDEK, L.D. 1988 Film drop production as a function of bubble size. *J. Geophys. Res.: Oceans* **93** (C4), 3649–3654.

BLANCO–RODRÍGUEZ, F.J. & GORDILLO, J.M. 2020 On the sea spray aerosol originated from bubble bursting jets. *J. Fluid Mech.* **886**, R2.

BRASZ, C.F., BARTLETT, C.T., WALLS, P.L.L., FLYNN, E.G., YU, Y.E. & BIRD, J.C. 2018 Minimum size for the top jet drop from a bursting bubble. *Phys. Rev. Fluids* **3** (7), 074001.

BURROWS, S.M., OGUNRO, O., FROSSARD, A.A., RUSSELL, L.M., RASCH, P.J. & ELLIOTT, S.M. 2014 A physically based framework for modeling the organic fractionation of sea spray aerosol from bubble film Langmuir equilibria. *Atmos. Chem. Phys.* **14** (24), 13601–13629.

CIPRIANO, R.J. & BLANCHARD, D.C. 1981 Bubble and aerosol spectra produced by a laboratory breaking wave. *J. Geophys. Res.: Oceans* **86** (C9), 8085–8092.

CLIFT, R., GRACE, J. & WEBER, M. 1978 *Bubbles, drops, and particles. Bubbles Drops Particles*. Academic Press, Inc.

COCHRAN, R.E., RYDER, O.S., GRASSIAN, V.H. & PRATHER, K.A. 2017 Sea spray aerosol: the chemical link between the oceans, atmosphere, and climate. *Accounts Chem. Res.* **50** (3), 599–604.

DEANE, G.B., STOKES, M.D. 2002 Scale dependence of bubble creation mechanisms in breaking waves. *Nature* **418** (6900), 839–844.

DEIKE, LUC 2022 Mass transfer at the ocean–atmosphere interface: the role of wave breaking, droplets, and bubbles. *Annu. Rev. Fluid Mech.* **54** (2022), 191–224.

DEIKE, L., GHABACHE, E., LIGER-BELAIR, G., DAS, A.K., ZALESKI, S., POPINET, S. & SÉON, T. 2018 Dynamics of jets produced by bursting bubbles. *Phys. Review Fluids* **3** (1), 013603.

DEIKE, L., LENAIN, L. & MELVILLE, W.K. 2017 Air entrainment by breaking waves. *Geophys. Res. Lett.* **44** (8), 3779–3787.

DEIKE, L., MELVILLE, W.K. & POPINET, S. 2016 Air entrainment and bubble statistics in breaking waves. *J. Fluid Mech.* **801**, 91–129.

DEIKE, L., REICHL, B.G. & PAULOT, F. 2022 A mechanistic sea spray generation function based on the sea state and the physics of bubble bursting. *AGU Adv.* **3** (6), e2022AV000750.

DUBITSKY, L., STOKES, M.D., DEANE, G.B. & BIRD, J.C. 2023 Effects of salinity beyond coalescence on submicron aerosol distributions. *J. Geophys. Res.: Atmospheres* **128** (10), e2022JD038222.

ERININ, M.A., NÉEL, B., MAZZATENTA, M.T., DUNCAN, J.H. & DEIKE, L. 2023 Comparison between shadow imaging and in-line holography for measuring droplet size distributions. *Exp. Fluids* **64** (5), 96.

ERININ, M.A., WANG, S.D., LIU, R., TOWLE, D., LIU, X. & DUNCAN, J.H. 2019 Spray generation by a plunging breaker. *Geophys. Res. Lett.* **46** (14), 8244–8251.

FIROUZI, M., HOWES, T. & NGUYEN, A.V. 2015 A quantitative review of the transition salt concentration for inhibiting bubble coalescence. *Adv. Colloid Interface* **222**, 305–318.

FORESTIERI, S.D., MOORE, K.A., MARTINEZ BORRERO, R., WANG, A., STOKES, M.D. & CAPPA, C.D. 2018 Temperature and composition dependence of sea spray aerosol production. *Geophys. Res. Lett.* **45** (14), 7218–7225.

FROSSARD, A.A. *et al.* 2019 Marine aerosol production via detrainment of bubble plumes generated in natural seawater with a forced-air venturi. *J. Geophys. Res.: Atmos.* **124** (20), 10931–10950.

GAO, Q., DEANE, G.B. & SHEN, L. 2021 Bubble production by air filament and cavity breakup in plunging breaking wave crests. *J. Fluid Mech.* **929**, A44.

GAÑÁN-CALVO, A.M. 2017 Revision of bubble bursting: universal scaling laws of top jet drop size and speed. *Phys. Rev. Lett.* **119** (20), 204502.

GAÑÁN-CALVO A.M. 2023 The ocean fine spray. *Phys. Fluids* **35** (2), 023317.

GHABACHE, E., ANTKOWIAK, A., JOSSERAND, C. & SÉON, T. 2014 On the physics of fizziness: how bubble bursting controls droplets ejection. *Phys. Fluids* **26** (12), 121701.

GHABACHE, E. & SÉON, T. 2016 Size of the top jet drop produced by bubble bursting. *Phys. Rev. Fluids* **1** (5), 051901.

JIANG, X., ROTILY, L., VILLERMAUX, E. & WANG, X. 2022 Submicron drops from flapping bursting bubbles. *Proc. Natl Acad. Sci. USA* **119** (1), e2112924119.

JIANG X., ROTILY L., VILLERMAUX E. & WANG X. 2024 Abyss aerosols: drop production from underwater bubble collisions. *Phys. Rev. Lett.* **133** (2), 024001.

DE LEEUW, G., ANDREAS, E.L., ANGUELOVA, M.D., FAIRALL, C.W., LEWIS, E.R., O'DOWD, C., SCHULZ, M. & SCHWARTZ, S.E. 2011 Production flux of sea spray aerosol. *Rev. Geophys.* **49**, 2010RG000349.

LEWIS, E.R. & SCHWARTZ, S.E. 2004 *Sea Salt Aerosol Production: Mechanisms, Methods, Measurements, and Models*. American Geophysical Union.

LHUISSIER, H. & VILLERMAUX, E. 2012 Bursting bubble aerosols. *J. Fluid Mech.* **696**, 5–44.

LIGER-BELAIR, G. & JEANDET, P. 2003 Capillary-driven flower-shaped structures around bubbles collapsing in a bubble raft at the surface of a liquid of low viscosity. *Langmuir* **19** (14), 5771–5779.

LIU, Z., FARSOIYA, P.K., PERRARD, S. & DEIKE, L. 2024 Direct numerical simulation of bubble rising in turbulence. *J. Fluid Mech.* **999**, A11.

MODINI, R.L., RUSSELL, L.M., DEANE, G.B. & STOKES, M.D. 2013 Effect of soluble surfactant on bubble persistence and bubble-produced aerosol particles. *J. Geophys. Res.: Atmos.* **118** (3), 1388–1400.

MOSTERT, W., POPINET, S. & DEIKE, L. 2022 High-resolution direct simulation of deep water breaking waves: transition to turbulence, bubbles and droplets production. *J. Fluid Mech.* **942**, A27.

MÅRTENSSON, E.M., NILSSON, E.D., DE LEEUW, G., COHEN, L.H. & HANSSON, H.-C. 2003 Laboratory simulations and parameterization of the primary marine aerosol production. *J. Geophys. Res.: Atmos.* **108** (D9), 2002JD002263.

NÉEL, B. & DEIKE, L. 2021 Collective bursting of free-surface bubbles, and the role of surface contamination. *J. Fluid Mech.* **917**, A46.

NÉEL, B. & DEIKE, L. 2022 Velocity and size quantification of drops in single and collective bursting bubbles experiments. *Phys. Rev. Fluids* **7** (10), 103603.

NÉEL, B., ERININ, M.A. & DEIKE, L. 2022 Role of contamination in optimal droplet production by collective bubble bursting. *Geophys. Res. Lett.* **49** (1), 103603.

PAULOT, F., PAYNTER, D., WINTON, M., GINOUX, P., ZHAO, M. & HOROWITZ, L.W. 2020 Revisiting the impact of sea salt on climate sensitivity. *Geophys. Res. Lett.* **47** (3), e2019GL085601.

POULAIN, S., VILLERMAUX, E. & BOUROUIBA, L. 2018 Ageing and burst of surface bubbles. *J. Fluid Mech.* **851**, 636–671.

PRATHER, K.A., *et al.* 2013 Bringing the ocean into the laboratory to probe the chemical complexity of sea spray aerosol.. *Proc. Natl Acad. Sci. USA* **110** (19), 7550–7555.

RESCH, F. & AFETI, G. 1991 Film drop distributions from bubbles bursting in seawater. *J. Geophys. Res.: Oceans* **96** (C6), 10681–10688.

RESCH, F. & AFETI, G. 1992 Submicron film drop production by bubbles in seawater. *J. Geophys. Res.: Oceans* **97** (C3), 3679–3683.

RUTH, D.J., AIYER, A.K., RIVIÈRE, A., PERRARD, S. & DEIKE, L. 2022 Experimental observations and modelling of sub-Hinze bubble production by turbulent bubble break-up. *J. Fluid Mech.* **951**, A32.

RUTH, D.J., VERNET, M., PERRARD, S. & DEIKE, L. 2021 The effect of nonlinear drag on the rise velocity of bubbles in turbulence. *J. Fluid Mech.* **924**, A2.

SAMPATH, K., AFSHAR-MOHAJER, N., CHANDRALA, L.D., HEO, W-S, GILBERT, J., AUSTIN, D., KOEHLER, K. & KATZ, J. 2019 Aerosolization of crude oil-dispersant slicks due to bubble bursting. *J. Geophys. Res.: Atmos.* **124** (10), 5555–5578.

SELLEGRI, K., O'DOWD, C.D., YOON, Y.J., JENNINGS, S.G. & DE LEEUW, G. 2006, Surfactants and submicron sea spray generation. *J. Geophys. Res.: Atmos.* **111** (D22).

SÉON, T. & LIGER-BELAIR, G. 2017 Effervescence in champagne and sparkling wines: from bubble bursting to droplet evaporation. *Eur. Phys. J. Special Topics* **226** (1), 117–156.

SHAW D.B. & DEIKE L. 2024 Film drop production over a wide range of liquid conditions. *Phys. Rev. Fluids* **9** (3), 033602.

SHETTLE, E. & FENN, R. 1979 Models for the aerosols of the lower atmosphere and the effects of humidity variations on their optical properties. *Environ. Res.* **676**, 94.

SPIEL, D.E. 1997*a* A hypothesis concerning the peak in film drop production as a function of bubble size. *J. Geophys. Res.: Oceans* **102** (C1), 1153–1161.

SPIEL, D.E. 1997*b* More on the births of jet drops from bubbles bursting on seawater surfaces. *J. Geophys. Res.: Oceans* **102** (C3), 5815–5821.

SPIEL, D.E. 1998 On the births of film drops from bubbles bursting on seawater surfaces. *J. Geophys. Res.: Oceans* **103** (C11), 24907–24918.

TOBA, Y. 1959 Drop production by bursting of air bubbles on the sea surface (ii) theoretical study on the shape of floating bubbles. *J. Oceanogr. Soc. Jpn.* **15** (3), 121–130.

TYREE, C.A., HELLION, V.M., ALEXANDROVA, O.A., ALLEN, J.O. 2007 Foam droplets generated from natural and artificial seawaters. *J. Geophys. Res.: Atmos.* **112** (D12).

VERON, F. 2015 Ocean spray. *Annu. Rev. Fluid Mech.* **47** (2015), 507–538.

WALLS, P.L.L., HENAUX, L. & BIRD, J.C. 2015 Jet drops from bursting bubbles: how gravity and viscosity couple to inhibit droplet production. *Phys. Rev. E* **92** (2), 021002.

WANG, X. 2017 The role of jet and film drops in controlling the mixing state of submicron sea spray aerosol particles. *Proc. Natl Acad. Sci. USA* **114** (27), 6978–6983.

WOOLF, D. & THORPE, S. 1991 Bubbles and the air-sea exchange of gases in near-saturation conditions. *J. Mar. Res.* **49** (3), 435–466.

ZINKE, J., NILSSON, E.D., ZIEGER, P. & SALTER, M.E. 2022 The effect of seawater salinity and seawater temperature on sea salt aerosol production. *J. Geophys. Res.: Atmos.* **127** (16), e2021JD036005.